

Detectability of Atmospheric Biosignatures in Earth Analogs with Varying Surface Boundary Conditions: Prospects for Characterization in the UV, Visible, Near-Infrared, and Mid-Infrared Regions

DIBYA BHARATI PRADHAN,^{1,2} PRIYANKUSH GHOSH,^{1,2} OOMMEN P. JOSE,^{1,2} AND LITON MAJUMDAR^{1,2}

¹*Exoplanets and Planetary Formation Group, School of Earth and Planetary Sciences, National Institute of Science Education and Research, Jatni 752050, Odisha, India*

²*Homi Bhabha National Institute, Training School Complex, Anushaktinagar, Mumbai 400094, India*

ABSTRACT

The search for potentially habitable exoplanets centers on detecting biosignature molecules in Earth-like atmospheres, which makes it essential to understand their detectability under biologically and geologically influenced conditions. In this study, we model the reflection and thermal emission spectra of such atmospheres across the UV/VIS/NIR and mid-IR regions and simulate their detectability with future mission concepts such as the Habitable Worlds Observatory (HWO) and the Large Interferometer for Exoplanets (LIFE). We employ Numerical Weather Prediction (NWP) model data, based on Earth's atmosphere, to derive temperature pressure profiles and couple them with a 1D photochemical model to assess the detectability of these molecules in Earth analogs located 10 parsecs away. We investigate the dominant reaction pathways and their contributions to the atmospheric composition of an Earth analog, with a focus on how they shape the resulting molecular signatures. We also examine the role of surface boundary conditions, which indirectly trace the effects of biological and geological processes, on the detectability of these molecules using HWO- and LIFE-type mission concepts. Our findings indicate that O₃ is detectable with both mission concepts, while H₂O requires specific surface humidity levels for detection with LIFE and shows only potential detectability with HWO. CO₂ is detectable with LIFE. Both N₂O and CH₄ require continuous surface outgassing for potential detection with LIFE, and CH₄ further requires low surface humidity to prevent masking by water features. Our work highlights the feasibility of characterizing the atmospheres of Earth analogs in the UV/VIS/NIR and mid-IR domains using HWO- and LIFE-type mission concepts and offers guidance for the development of future missions operating in these spectral regions.

Keywords: Exoplanets (498); Exoplanet atmospheres (487); Exoplanet atmospheric structure (2310); Exoplanet atmospheric composition (2021)

1. INTRODUCTION

The discovery of over 6,000 exoplanets to date (NASA Exoplanet Archive¹) has significantly advanced the field of exoplanetary science, transforming our understanding of planetary systems beyond our own. This growing catalog of distant worlds underscores the importance of analyzing their atmospheres to gain insight into their underlying physical processes and chemical composition (Madhusudhan 2019). Observatories such as the Kepler Space Telescope, the Hubble Space Telescope (HST), and the James Webb Space Tele-

scope (JWST) have played a pivotal role in revealing the extraordinary diversity of exoplanets (Seager & Deming 2010; Sing et al. 2011; Fortney 2024). The Kepler mission, in particular, revolutionized our knowledge by identifying thousands of exoplanets and showcasing a wide variety of planetary types, from Earth-sized rocky worlds to gas giants, and exotic “super-Earths” and “mini-Neptunes” (Lissauer et al. 2014). Hubble and Spitzer, with their space-based infrared photometry and spectrophotometry, provided the first glimpses into the compositions of exoplanets, detecting water vapor, clouds, and other key atmospheric components (Charbonneau et al. 2002, 2008). More recently, JWST has furthered this exploration, offering unprecedented infrared sensitivity that enables scientists to study the atmospheres of smaller, cooler exoplanets in greater detail (Kempton et al. 2023; Greene et al. 2023).

Corresponding author: Liton Majumdar
 liton@niser.ac.in; dr.liton.majumdar@gmail.com

¹ <https://exoplanetarchive.ipac.caltech.edu/>

As the field advances, the focus is gradually shifting towards discovering Earth-sized planets and characterizing temperate terrestrial worlds, with a major objective being the search for potential biological signatures, commonly referred to as “biosignatures” in the astronomy and planetary science communities (Robinson et al. 2011; Alei et al. 2024). In the coming decades, efforts will be dedicated to refining detection methods to identify smaller, rocky planets within the habitable zones of their stars, where liquid water could exist. Research will also focus on studying the atmospheric properties of a large, statistically significant, and consistent observational sample of rocky exoplanets (Fujii et al. 2018). Direct imaging and spectroscopy are expected to be the primary methods to achieve this objective (Currie et al. 2023). Of all exoplanets discovered so far, only a handful have been successfully observed through direct imaging techniques (Zurlo 2024). This stark contrast highlights the challenges of directly imaging exoplanets, which often require advanced instrumentation and favorable conditions. However, direct imaging is the only technique that allows for direct capture of photons emitted by exoplanets, setting it apart from other detection methods (Marois et al. 2008; Lagrange et al. 2010; Zurlo 2024). Another way to directly image exoplanets, apart from using a coronagraph, is with a nulling interferometer (Bracewell 1978; Angel & Woolf 1997). This technique cancels out the star’s light and makes it easier to isolate the planet’s thermal emission (Quanz et al. 2022a,b). A nulling interferometer helps achieve better spatial resolution. This allows for a detailed study of planetary systems that would be difficult to observe with other methods.

Proposed future space-based mission concepts, such as the Large Interferometer for Exoplanets (LIFE)² and the Habitable Worlds Observatory (HWO)³, offer the potential to target planetary thermal emission spectra (Quanz et al. 2018; Defrère et al. 2018; Fujii et al. 2018; López-Morales et al. 2019; Quanz et al. 2021; Quanz et al. 2022b; Alei et al. 2022) and reflection spectra (National Academies of Sciences, Engineering, and Medicine 2021). The LIFE space observatory concept is primarily a nulling interferometer operating in the mid-infrared (Quanz et al. 2022c; Quanz et al. 2018, 2021; Quanz et al. 2022b), designed to explore the atmospheric properties of a significant number of terrestrial exoplanets. LIFE’s scientific focus aligns with the detection and characterization of temperate exoplanets in the mid-infrared, a potential topic for a future L-class mission in the ESA Science Program, as highlighted by ESA’s Voyage 2050 Senior Committee report⁴. On the other hand,

the Astro2020 Decadal Survey has recommended that NASA develop a large (~ 6 m inscribed diameter), stable, space-based infrared/optical/ultraviolet telescope capable of high-contrast imaging and spectroscopy as the next flagship observatory to search for biosignatures in habitable zone exoplanets, while simultaneously enabling transformative general astrophysics (National Academies of Sciences, Engineering, and Medicine 2021).

The HWO and LIFE mission concepts focus on different wavelength regions, with HWO targeting the ultraviolet, visible, and near-infrared (UV/VIS/NIR) range of approximately 0.15 to 2 microns, while LIFE targets the mid-infrared (mid-IR) range of approximately 4 to 18.5 microns, primarily to study the atmospheres of temperate terrestrial exoplanets and provide complementary insights into planetary physics and chemistry. These missions collectively improve our ability to detect key biosignatures, refine planet characterization techniques, and produce complementary scientific results (Alei et al. 2024). For example, reflected light observations provide information on a planet’s dynamics, cloud composition, albedo, surface biosignatures, and ocean glint (Sagan et al. 1993; Williams & Gaidos 2008; Alei et al. 2024). However, this method faces challenges, such as the strong correlation between radius and albedo in the presence of clouds, which complicates data interpretation. In contrast, thermal emission observations directly measure planetary radiation, offering insights into thermal structure and atmospheric composition, while being less affected by patchy clouds and providing more accurate radius measurements (Alei et al. 2022; Alei et al. 2024).

Several efforts have been made to study the reflection and thermal emission spectra of terrestrial exoplanets. Notably, the work of Alei et al. (2024) stands out as the most recent study focusing on single-instrument and joint retrievals, highlighting both the HWO and LIFE concepts. The potential detection capabilities of a mission like LIFE have been well explored in studies by Quanz et al. (2022b); Dannert et al. (2022); Kammerer et al. (2022). The LIFE paper series has also extensively addressed the forward modeling (Schwieterman et al. 2022; Schwieterman & Leung 2024; Angerhausen et al. 2024) and retrieval of thermal emission spectra (Alei et al. 2022; Konrad et al. 2022; Konrad et al. 2023). However, there have not been many direct studies of HWO simulations considering a proper instrumental setup, except for a few Alei et al. (2024); Young et al. (2024). The focus of Young et al. (2024) is on the use of atmospheric retrieval models within a decision tree framework to analyze Earth-like exoplanets. The framework in the paper is designed to help identify biosignatures and planetary characteristics, specifically targeting modern Earth-like and Archean Earth-like analogs. Feng et al. (2018) presents the observed planet-star flux ratio, considering an albedo model and integrating it

² <https://life-space-mission.com/>

³ <https://habitableworldsobservatory.org/home>

⁴ <https://www.cosmos.esa.int/web/voyage-2050>

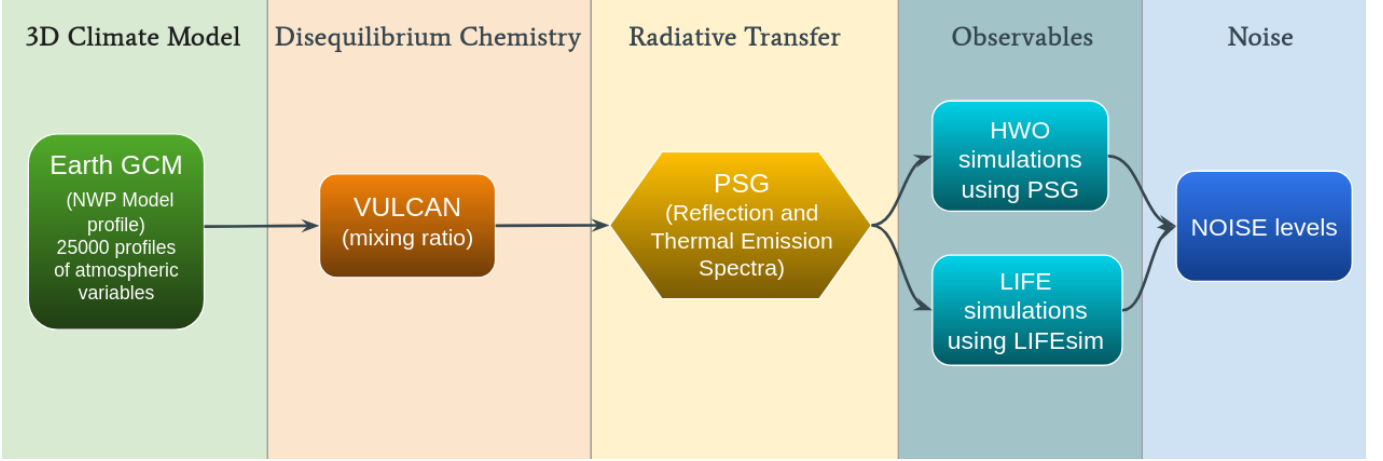


Figure 1. Flowchart representing our methodical pipeline. The model types are indicated in the large boxes: green for climate model, peach for chemistry model, yellow for radiative transfer model, cyan for observables simulator, and blue for noise output. These models are interconnected. The reflection spectra and thermal emission spectra represent the overall outputs of the pipeline, leading to the spectra that will be observed by future HWO and LIFE missions.

with a direct imaging noise simulator while also conducting a retrieval study. Other notable retrieval studies include [Damianno & Hu \(2022\)](#); [Robinson & Salvador \(2023\)](#); [Latouf et al. \(2023, 2024\)](#), primarily focusing on Earth twin studies for the Habitable Exoplanet Observatory (HabEx) and the Large Ultraviolet Optical Infrared Surveyor (LUVOIR) concepts.

Earth is the best example of a habitable and inhabited world ([Robinson & Reinhard 2019](#)). To identify a distant habitable world, it is important to model a planet as an Earth analog with varying surface boundary conditions to indirectly reflect active biological and geological processes, which play a fundamental role in regulating atmospheric composition. To understand the role of these mechanisms, we use data from the ECMWF-IFS model, a high-resolution Earth General Circulation Model (GCM) employed for numerical weather prediction (NWP), to obtain temperature-pressure (T-P) profiles. These profiles are then coupled with the 1D chemical kinetics model VULCAN to investigate the detectability of molecules influenced by surface boundary conditions. Our analysis focuses on their potential observability in the UV/VIS/NIR and mid-IR regions. We are using the scientific concepts laid out by the HWO and LIFE mission concepts as a foundation for our study of an Earth-analog located at a distance of 10 parsecs. This work would also help to consider the broader applicability to other future missions that aim to characterize terrestrial exoplanets in the UV, VIS, NIR, and mid-IR regions.

The structure of the paper is as follows: In Section 2, we outline the workflow of the study, detailing the models used and the parameters adopted. The NWP model data, the chemical kinetics model with network updates, the approach taken for our simulations with different boundary conditions, and the models used for observation simulations, including their noise parameters, are all described here. The kinetics model

output is presented in Section 3, where we elaborate on the major chemical processes in the different layers of the atmosphere and present synthetic observations for all the simulations whose methodologies were covered in the previous section. The results are twofold: the reflection spectra to be obtained by HWO and the thermal emission spectra to be acquired by LIFE. We address the outputs of the simulations with various boundary conditions. We elaborate further on this topic in the section that follows, i.e., Section 4. We compare and explain the visible features and complementary nature of HWO and LIFE, along with the limitations of this study. Finally, our findings are drawn in Section 5.

2. METHODS

To simulate Earth-like atmospheric conditions under disequilibrium chemistry, obtain both reflection and thermal emission spectra, and analyze the detectability of molecular features using the upcoming Habitable Worlds Observatory (HWO) and Large Interferometer for Exoplanets (LIFE) mission concepts, we have followed the methodology described in the flow chart illustrated in Figure 1. In this section, we provide a detailed description of the models used and the procedures followed, starting with the data from NWP (Section 2.1), followed by the chemical kinetic model (Section 2.2), and the reflection and thermal emission spectrum simulator (Section 2.3), along with the noise parameters (Section 2.4).

2.1. Numerical Weather Prediction Model (NWP): Understanding the Thermal Structure

We obtain data for the temperature profiles, as shown in Figure 2, from the latest version of the atmospheric profile database of the forecasting system of the European Centre

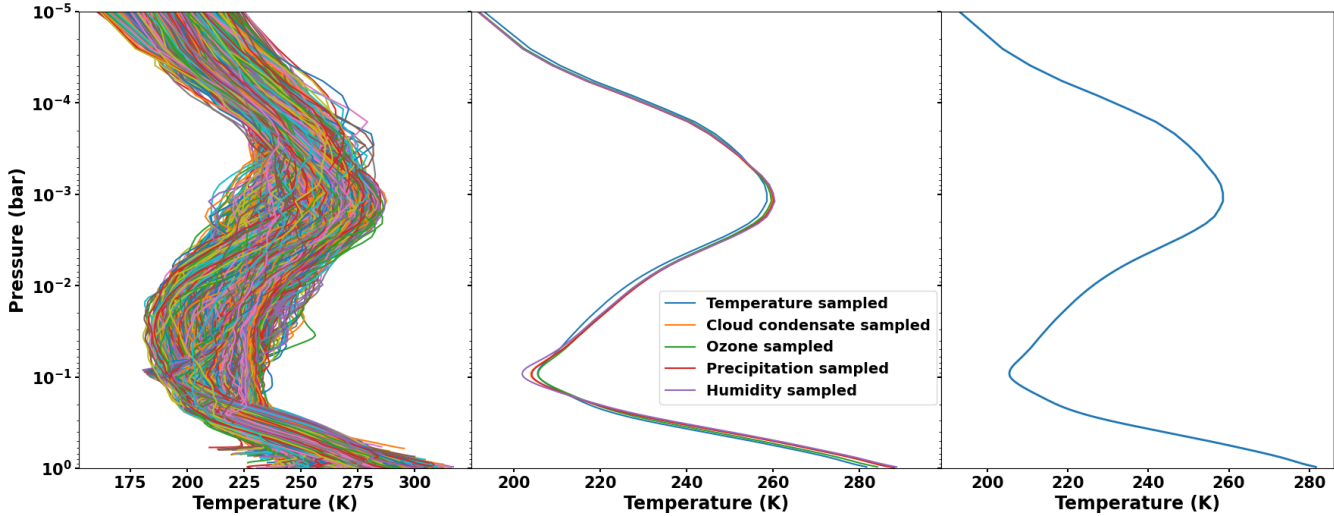


Figure 2. 5000 temperature-pressure (T-P) profiles derived from a numerical weather prediction (NWP) model (left), an average T-P profile considering all five types of sampling techniques (middle), and the mean temperature-pressure profile representing the global average conditions of modern Earth (right). The leftmost panel illustrates the variability in T-P profiles due to different atmospheric conditions captured by the NWP model, while the far right panel provides a single, averaged T-P profile that can serve as a reference for global atmospheric studies of an Earth analog. The global average T-P profile remains the same across all our models: M1, M2, M3, M4, and M5.

for Medium-range Weather Forecasts (ECMWF)⁵. This data is generated from the Numerical Weather Prediction (NWP) model. Its Satellite Application Facility (NWP SAF) periodically produces datasets that contain sample profiles of atmospheric variables extracted from forecasting models.

The latest version of the NWP model data comprises 25,000 atmospheric profiles sourced from globally operational short-range forecasts, typically covering time frames from a few hours to 3 days. This dataset captures normal conditions, typical variability, and extreme scenarios of atmospheric behavior on Earth. The short-range forecasts span from September 1, 2013, to August 31, 2014, and are generated four times daily at 00:00, 06:00, 12:00, and 18:00 UTC. The data is structured across 137 vertical pressure levels, ranging from the surface up to 0.01 hPa, with grid points spaced 16 km apart. These forecasts are produced by version Cy40r1 of the Integrated Forecasting System (IFS), which became operational at ECMWF on 19th November 2013. The IFS is a data assimilation system and a global numerical model for the Earth system.

The IFS-137 database employs a sampling method very similar to the one described by Chevallier et al. (2006). The sampling technique is based on maximizing the squared inter-profile departure, D , given by the equation:

$$D = \sum_{k=1}^K \sum_{m=1}^M \left(\frac{\theta_{ik}(m) - \theta_{jk}(m)}{\sigma_k(m)} \right)^2 \quad (1)$$

⁵ <https://nwp-saf.eumetsat.int/site/software/atmospheric-profile-data/>

Here, k and m denote the indices for the variable and level, respectively. The values of variable k at level m in two different profiles are represented by $\theta_{ik}(m)$ and $\theta_{jk}(m)$. The variables and levels under consideration are denoted by K and M , and $\sigma_k(m)$ represents the standard deviation of variable k at level m . A profile is randomly selected from the available forecasts and stored in a separate list. The subsequent profile is then chosen from the forecast set and compared to the previously saved profile. If the deviation of the new profile exceeds that of the saved one, it replaces the previous profile in the list. To ensure a comprehensive representation of the input data without biasing towards the extremes, 90% of the profiles in the dataset are selected randomly, as suggested by Eresmaa & McNally (2014).

This 25,000-profile database is divided into five subsets, with each subset containing 5000 profiles. These five subsets are produced by sampling the corresponding five different parameters: temperature, specific humidity, ozone mixing ratio (sampled using univariate sampling by using $K = 1$ in Eq. (1)), cloud condensate, and precipitation (sampled using bivariate sampling by using $K = 2$ in Eq. (1)).

Out of the five sampling techniques used in the dataset, we are only considering the 5000 profiles that are temperature-sampled (shown in Figure 2) since we are only dealing with T-P profiles for our work. We also checked with all the other sampling techniques by taking an average T-P profile. However, we did not find any difference in the mean T-P profile, as represented in Figure 2. So, we have used the temperature-sampled-average T-P profile for our work out of all the other sampling techniques. The averaging is done by grouping the temperature data for each pressure level. The averag-

ing is done to get a global average TP profile representative of Earth condition. Since the corresponding pressure values for each dataset are extremely close, the average of their corresponding temperature values remains approximately the same. This approximation is justified as each averaged (T, P) point is reasonably close to the subsequent one. The average T-P profile is shown in Figure 2. For the figures, the top of the atmosphere is taken at 10^{-5} bar and the bottom of the atmosphere at 1 bar.

The global average T-P profile remains the same across all our simulations. Varying surface conditions are incorporated by modifying the lower boundary conditions in the 1D chemical-kinetics model VULCAN, which is discussed in Section 2.2, using this same averaged T-P profile.

2.2. Chemical Kinetics Model VULCAN: Modelling the Evolution of Atmospheric Chemistry for Earth-like atmospheres under varying boundary conditions

2.2.1. Model Configuration

To determine the chemical abundances corresponding to the mean temperature-pressure (T-P) profile derived from the NWP model (shown in Figure 2), we coupled the mean T-P profile with VULCAN 2.0⁶, an open-source 1-D chemical kinetics code as described by Tsai et al. (2021). VULCAN solves the Eulerian continuity equation while incorporating the effects of condensation, advective transport, and chemical sources and sinks.

For our simulations, we considered 120 vertical layers, setting the pressure at the bottom to 1 bar and at the top to 5×10^{-8} bar. This configuration provides sufficient vertical resolution to accurately capture atmospheric processes across a broad range of pressures. For the initial state of the atmosphere, we used constant mixing ratio values reflective of modern Earth's composition (listed in Table 1) which VULCAN utilizes to initiate chemical kinetics for modern Earth. The default solar flux for Earth, adopted in VULCAN, is based on a high-resolution spectrum from Gueymard (2018). We also activated condensation and settling processes to capture the tropospheric cold trap. Above this region, the abundance of water vapor is influenced by diffusion from the lower troposphere and methane oxidation, providing a more accurate representation of upper atmospheric dynamics (Tsai et al. 2021). The other disequilibrium processes incorporated include eddy diffusion and molecular diffusion. The eddy diffusion is regulated by the eddy diffusion coefficient (K_{zz}) which is kept constant at $1 \times 10^5 \text{ cm}^2 \text{s}^{-1}$ as it is the average of the K_{zz} values considered for modern Earth in Tsai et al. (2021).

Table 1. Initial atmospheric composition, detailing the constant mixing ratio values based on modern Earth composition used to initialize the VULCAN model.

Species	Initial molecular mixing ratio
N_2	0.78
O_2	0.20
H_2O	10^{-6}
CO_2	4×10^{-4}
Ar	9.34×10^{-3}
SO_2	2×10^{-10}

2.2.2. Adding reactions to the chemical network

For our analysis, we have used the SNCHO Full Photo Network which is the chemical network used in Tsai et al. (2021) to benchmark modern Earth-like atmosphere. This network includes 96 species linked with 570 forward thermochemical reactions and 69 photodissociation branches. We extended this network by incorporating the reactions associated with HO_2NO_2 listed in Table 2. These reactions were taken from the chemical network used in ATMOS, a chemical kinetics code optimized for terrestrial exoplanets, as detailed by Arney et al. (2014).

These additional reactions primarily influence the photochemistry of the HO_x and NO_x families, particularly at higher altitudes or in regions characterized by lower temperatures. H_2O , NO_2 , and O_2 are among the key molecules of focus in our study. Given that the added reactions involve the formation of these species, we anticipate that their chemistry may vary as a result of these reactions.

2.2.3. The importance of surface boundary conditions and the initial composition

Boundary conditions are critical for understanding the planetary processes occurring near the surface and at the top of the atmosphere, as they play a significant role in shaping the atmospheric composition and dynamics. For the lower boundary conditions, sources and sinks are quantified by flux, mixing ratio, and (dry/wet) deposition velocities. Fluxes represent surface emission, while deposition rates dictate the removal of gases from the atmosphere at the lower boundary through processes such as gas absorption or uptake by the surface (Hu et al. 2012). For rocky planets, constant fluxes are typically assumed. The dry deposition velocity v_d of gases is calculated using the formula provided by Wesely (1989):

$$v_d = \frac{-F_c}{C_z} \quad (2)$$

Here, F_c is the flux density and C_z is the concentration at height z .

⁶ <https://github.com/exoclime/VULCAN>

Table 2. Reactions added to the SNCHO full photo chemical network for VULCAN.

Reaction	Rates	References
$O + HO_2NO_2 \rightarrow OH + NO_2 + O_2$	$7.80 \times 10^{-11} \exp^{-\frac{3400}{T}}$	(Chang et al. 1981)
$OH + HO_2NO_2 \rightarrow H_2O + NO_2 + O_2$	$1.3 \times 10^{-12} \exp^{\frac{380}{T}}$	(MacLeod et al. 1988), (Smith et al. 1984), (Barnes et al. 1981), (Barnes et al. 1982)
$HO_2 + NO_2 + M \rightarrow HO_2NO_2 + M$	$1.9 \times 10^{-31} T^{4 \times 10^{-12}} \exp^{-\frac{3.4}{T}}$	IUPAC-04 (Atkinson et al. 2004)
$HO_2NO_2 + h\nu \rightarrow HO_2 + NO_2$	by photolysis cross section	SwRI ^a (Huebner & Carpenter 1979), (Huebner et al. 1992)
$HO_2NO_2 + h\nu \rightarrow OH + NO_3$	by photolysis cross section	SwRI ^a (Huebner & Carpenter 1979), (Huebner et al. 1992)

^a <https://phidrates.space.swri.edu/>

For our simulations, we consider surface emission and deposition rates for different species at the lower boundary conditions, utilizing the modern Earth benchmark from Tsai et al. (2021). This approach ensures that the model accurately reflects the influence of surface interactions on atmospheric chemical processes. In VULCAN, if the boundary condition for a particular molecule is not specified, a zero-flux condition is assumed (Tsai et al. 2021).

VULCAN’s default surface boundary fluxes and deposition rates for modern Earth-like atmospheres include a variety of molecules. Among them, for N_2O and CH_4 , only outgassing flux is considered, with deposition set to zero. For H_2O and CO_2 , neither flux nor deposition is considered; instead, their mixing ratios are fixed at the surface. In addition to these default boundary conditions in VULCAN, we have introduced boundary values for CO_2 and O_2 in our simulations. The CO_2 flux and deposition rates are derived from ATMOS (Arney et al. 2014). For O_2 , we consider a flux value of 7.1×10^9 molecules $cm^{-2} s^{-1}$, which is derived from geochemical processes involving the subduction of Fe^{3+} into the mantle over the past 4 billion years (Catling et al. 2001; Kleinböhl et al. 2018). Since an established deposition rate for oxygen is unavailable in the literature, we assumed a value similar to that of CO_2 , using $1 \times 10^{-6} cm s^{-1}$.

2.2.4. The Earth-like Models with varying boundary conditions

In our simulation, we investigated five distinct cases for Earth-like exoplanets, labeled as Models M1 through M5, as detailed in Table 3. The primary model, described in Section 2.2.1, serves as the benchmark for present-day Earth, as outlined by Tsai et al. (2021). In this model, we consider the default boundary conditions with fixed surface mixing ratios for both H_2O and CO_2 .

The subsequent models, M1 through M5 vary in terms of their boundary conditions and whether additional surface fluxes and deposition velocities for CO_2 and O_2 are included. All these models have also been checked against the benchmarked modern Earth case in Section 2.2.1.

For Models M1 and M2, we assessed the impact of maintaining fixed surface abundances for CO_2 and H_2O , excluding boundary values for other species. In VULCAN, the surface water vapor mixing ratio is set to 0.00894, which equates to 25% relative humidity. Moreover, CO_2 levels are fixed at 400 ppm since VULCAN does not factor in key processes that influence CO_2 concentrations, such as biological activity, interactions with oceans, and geological processes (Tsai et al. 2021). This led us to evaluate the sensitivity of these two species in Models M1 and M2. Next in model M3, we incorporated the default boundary values for other species, as presented in Table 2 of Tsai et al. (2021). However, unlike the main model, which fixes the mixing ratios for H_2O and CO_2 at the surface, model M3 allows these mixing ratios to vary. Finally, for M4 and M5, we introduced CO_2 boundary values from ATMOS (Arney et al. 2014) and flux for O_2 from Kleinböhl et al. (2018) as mentioned in Section 2.2.3. And, we then switched the sink (i.e., deposition velocity) on and off to assess its effect on the model outputs. A comprehensive analysis of the results from these models is provided in Section 3.4 and 3.5.

2.3. Planetary Spectrum Generator (PSG): Simulating Reflection and Thermal Emission Spectra

The radiance spectra for the mean temperature-pressure profile is generated by coupling the time-evolved chemical abundances from VULCAN to the radiative transfer suite Planetary Spectrum Generator (PSG)⁷ (Villanueva et al. 2018). It is a versatile and publicly accessible online radiative-transfer tool designed to simulate the remote spectral observables of planetary bodies across a wide range of viewing angles and distances (Villanueva et al. 2018; Villanueva et al. 2022). The PSG model uses the HITRAN 2020 database to obtain its input opacities (Gordon et al. 2022). In our study, PSG was employed to create reflection and thermal emission spectra based on our average temperature-pressure profile and cor-

⁷ <https://psg.gsfc.nasa.gov/>

Table 3. Summary of Earth-like atmosphere models with constant initial atmosphere and varying boundary conditions.

Models	Composition of atmosphere	Boundary Conditions		Fixed species at surface
		Flux (cm ⁻² s ⁻¹)	v (dep)(cm s ⁻¹)	
M1	Modern Earth-like: N ₂ = 78%, O ₂ = 20%, CO ₂ =0.04%, H ₂ O=1× 10 ⁻⁴ %, Ar= 0.934%, SO ₂ = 2 × 10 ⁻⁸ %	No Boundary	No Boundary	Nil
M2		No Boundary	No Boundary	H ₂ O ^a , CO ₂ ^b
M3		Default Boundary	Default Boundary	Nil
M4		O ₂ = 7.1 × 10 ⁹ , CO ₂ = 6.875 × 10 ⁸	O ₂ = 0, CO ₂ = 5 × 10 ⁻⁵	H ₂ O ^a
M5		O ₂ = 7.1 × 10 ⁹ , CO ₂ = 6.875 × 10 ⁸	O ₂ = 1 × 10 ⁻⁶ , CO ₂ = 5 × 10 ⁻⁵	H ₂ O ^a

^a H₂O = 0.00894^b CO₂ = 4 × 10⁻⁴

responding chemical compositions outlined earlier. The parameters used to simulate reflection and thermal emission spectra for modern Earth-like exoplanets are provided in Table 4. The spectra were simulated for a wavelength range of 0.1 - 2 μm for HWO simulations and 4 - 18.5 μm for LIFE simulations. All simulations in this work involving PSG assume a phase angle of 77.8°, consistent with the approach used by Alei et al. (2024). Instead of modeling reflected light across the full planetary disk, we adopt a Lambertian surface and use a fixed average solar zenith angle of 77.756° to approximate conditions near quadrature. This method provides realistic results with a single simulation, following the methodology described by Alei et al. (2024). All simulations in this study are performed under cloud-free conditions and assume a wavelength-independent surface albedo.

2.4. Noise Calculations for HWO and LIFE

2.4.1. PSG: Noise Calculations and Observation Simulation for HWO

PSG includes a noise simulator capable of computing noise and sensitivity for a wide range of detectors and instrument configurations. In this work, we used PSG to simulate reflection spectra along with the expected noise levels detectable by HWO. The configuration parameters used to model noise for HWO are detailed in Table 5. These instrument parameters are derived from the specifications outlined by National Academies of Sciences, Engineering, and Medicine (2021).

The considered wavelength range spans 0.15–2 μm, with a telescope diameter of 6 meters. For noise calculations, we adopt a resolving power R of 7 between 0.15–0.51 μm, $R = 140$ between 0.51–1 μm, and $R = 70$ between 1–2.0 μm for HWO, in accordance with values from the LUVOIR-B concept as discussed by Alei et al. (2024). We assume an observation time of 100 hours to simulate the reflection spectra for all our models.

To benchmark our noise simulation for HWO against Alei et al. (2024), we scaled the noise and calibrated the reflected spectra to achieve a target signal-to-noise ratio (S/N) across three wavelength intervals: 0.15–0.51 μm (UV), 0.51–1 μm (VIS), and 1–2 μm (NIR). Specifically, we ensured an S/N of 10 at three reference wavelengths, 0.35 μm (UV), 0.55 μm (VIS), and 1.2 μm (NIR), and scaled the S/N across the remaining spectral range accordingly. Additionally, we generated 1 σ and 2 σ noise regions to represent the uncertainty across the spectrum.

As shown in Figure 4, the magnitude of the flux and the corresponding noise closely match the results of Alei et al. (2024), demonstrating excellent agreement.

2.4.2. LIFEsim: Noise Calculations and Observation Simulation for LIFE

LIFEsim is a state-of-the-art simulator specifically designed for the LIFE mission concept, providing accurate and reliable simulations of the interferometric measurement processes involved in its operation. This tool enables us to assess the capabilities of LIFE and explore the parameter space for the detection and characterization of exoplanets (Dannert et al. 2022). In our study, we input the theoretical thermal emission spectrum obtained from PSG into LIFEsim to generate noise and simulate observations for LIFE.

Since our study focuses on temperate terrestrial “Earth-like” planets, we assume the planet’s radius, surface gravity, and angular separation to be the same as those of Earth in the Sun-Earth system ($R = 6378.14$ km, ang. sep. = 0.1 arcsec, and $g = 9.8$ m s⁻²). The star-planet system is simulated at a distance of 10 parsecs. The simulation parameters used in LIFEsim are detailed in Table 6.

We consider LIFEsim in its “baseline” setup, which includes four collector apertures, each with a diameter of 2 m, a broadband wavelength range of 4 to 18.5 μm, a throughput of 5%, and a spectral resolution of $R = 50$ (Quanz et al. 2022b; Dannert et al. 2022). For the noise parameters, we adopt the

Table 4. Parameters that were used in PSG for generating emission and reflection spectra. The stellar and planetary parameters were taken to represent a modern Earth analog around a sun-like star.

PSG parameters	Emission & Reflection spectra
Stellar parameters	
Star temperature	5778 K
Radius	$1 R_{\odot}$
Semi-major axis	0.9837 AU
Star type	G-type
Planetary parameters	
Radius	$1 R_{\oplus}$
Distance	10 pc
Phase	77.8°
Surface and Atmospheric parameters	
Surface pressure	1013 mbar
Surface temperature	288 K
Albedo	0.3
Emissivity	0.692
Mean mol. weight	28.97 g/mol

Table 5. Noise parameters considered for simulations for HWO using PSG.

PSG parameters	HWO simulations
Aperture diameter	6 m
Spectral resolution	7, 140, 70
Wavelength range	0.15 μm – 2 μm
Beam (FWHM)	0.045 arcsec
Exozodi	4.5 local zodi
Contrast	10^{-10}
Exposure	3600 secs
Number of exposures	100
Number of pixels	10
Temperature of the optics	273 K
Emissivity of the optics	0.1
Inner working angle (IWA)	$3.73 \lambda/D$

baseline resolution of the instrument. All the configuration

parameters for noise, except for the exozodiacal dust level and spectral resolution, align with previous studies on LIFE. We assume the exozodiacal dust level to be 4.5 times the local zodiacal dust level, consistent with the approach taken by Alei et al. (2024).

Angerhausen et al. (2024) calculated how long certain molecular features (such as N_2O and CH_3X) in the thermal emission spectra of an Earth-like exoplanet around a Sun-like star at a distance of 5 pc would take to become distinguishable by varying the integration periods. They concluded that a 10-day observation period is relatively short, making it suitable for characterizing a larger sample of planets. A 50-day observation allows for a more thorough analysis, while a 100-day observation is optimistic and primarily applicable to the most promising targets for LIFE. Thus, in our study, we modeled the detectability of different molecules by considering a fixed observation duration of 50 days—an intermediate case from Angerhausen et al. (2024)—which also closely matches the required observation time for an Earth-twin at 10 pc for a nominal setup of $R = 50$, $\text{S/N} = 10$, and a 2m aperture diameter, as presented in Table 6 of Konrad et al. (2022).

To benchmark our noise simulation for LIFE against Alei et al. (2024), we consider a fixed S/N of 10 at 11.2 μm , for the thermal emission spectra. As shown in Figure 5, the magnitude of the flux and the corresponding noise closely match the results of Alei et al. (2024), demonstrating excellent agreement for LIFE noise calculations as well.

2.4.3. Metric for Molecular Detectability in HWO and LIFE

For our analysis, we assess the detectability of spectral features using a key metric: the band-integrated signal-to-noise ratio (SNR), computed following the approach of Angerhausen et al. (2024).

$$\text{SNR} = \sqrt{\sum_{i=1}^n \left(\frac{\Delta y_i}{\sigma(y_i)} \right)^2} \quad (3)$$

Here, Δy_i denotes the flux difference between two spectra: one including the target spectral feature and the other excluding it, for each of the n spectral bins. The term $\sigma(y_i)$ represents the instrumental noise in the same bin, determined from the observational sensitivity. For this noise term, we use the actual noise output from PSG for HWO spectra without any rescaling, and the corresponding noise values provided by the LIFEsim simulator for LIFE spectra. The resulting band-integrated SNR values for all molecular features are listed in Table 8, and the related analysis is discussed in Section 4.

As prescribed by Angerhausen et al. (2024), for N_2O and certain other molecules in LIFE spectra, considering an Earth-like planet 5 pc away orbiting a Sun-like star, a spectral feature is considered distinguishable if the band-integrated SNR exceeds a threshold of 5–10. In this work, for

a planet located 10 pc away around a Sun-like star, we tabulate the band-integrated SNR for different molecular features for HWO and LIFE. A molecule is considered detectable if the band-integrated SNR meets or exceeds the cited threshold range. Throughout this work, we adopt the following detectability convention for the band-integrated SNR (see equation 3): Detectable if $\text{SNR} \geq 10$, Potentially or marginally detectable if $5 \leq \text{SNR} < 10$, and Not detectable if $\text{SNR} < 5$. All detection statements are conditional on the assumed instrument setups and integration times.

Table 6. Parameters considered for simulations for LIFE using LIFEsim. For detailed explanations of the parameters, refer to (Dannert et al. 2022).

LIFEsim parameters	LIFE simulations
Collector aperture diameter	2 m
Spectral resolution	50
Wavelength range	4 μm – 18.5 μm
Elliptic latitude	0.78 rad
Exozodi	4.5 local zodi
Planet radius	$1 R_{\oplus}$
Star radius	$1 R_{\odot}$
Target distance	10 pc
Stellar effective temperature	5778 K
Angular separation	0.1 arcsec
Array baseline	optimized for planet
Integration time	50 days
Quantum efficiency	70%
Photon throughput	5%
Nulling baseline length	10-100 m
Array baseline ratio	6:1
Slew rate	10 hr
Time efficiency	80%

3. RESULTS

This section presents the output from the chemical kinetics model discussed in Section 2.2 and highlights the major chemical processes occurring in different atmospheric layers for a modern Earth-like benchmark. Following this, we discuss the simulations of the reflection spectra in the UV/VIS/NIR region for HWO in Section 3.2, as well as the thermal emission spectra in the mid-IR region for LIFE in Section 3.3, which are benchmarked against Alei et al. (2024). Finally, we examine different Earth-like model simu-

lations, introduced in Table 3, and their corresponding chemistry and spectra in Sections 3.4 and 3.5.

3.1. Atmospheric Chemistry: Depicting Chemical Processes using VULCAN

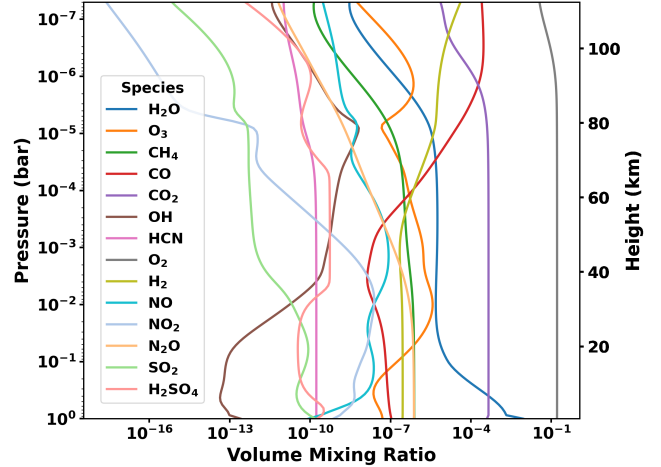


Figure 3. Mixing ratio profiles obtained from VULCAN for the temperature sampled average T-P profile. The molecules are H_2O , O_3 , CH_4 , CO , CO_2 , OH , HCN , O_2 , H_2 , NO , NO_2 , N_2O , SO_2 , H_2SO_4 . The molecules are selected considering their average mixing ratios $> 10^{-18}$ between 1 bar and 0.01 mbar.

Disequilibrium chemical processes play a major role in shaping the atmospheric composition of modern Earth. Our chemical kinetics model simulations capture the effects of these processes on the final evolved abundances.

Figure 3 presents the mixing ratio profiles simulated by VULCAN for the average temperature structure of modern Earth's atmosphere, derived from NWP model data (see Section 2.1). The species that play a crucial role in atmospheric chemistry and constitute the bulk composition of the atmosphere have volume mixing ratios (VMR) $\gtrsim 10^{-8}$ and serve as primary observable targets. To determine which chemical reactions significantly contribute to observable features in emission and reflection spectra, we examine different atmospheric layers from the surface to the uppermost regions.

We analyze all reactions across all atmospheric layers for molecules that exhibit observable features in the HWO and LIFE spectra.

To quantify the contribution of each major production and destruction reaction for every species, we calculate the percentage contribution of each reaction. The production or destruction percentage contribution of any reactant or product in a two-body reaction, such as $\text{A} + \text{B} \rightarrow \text{C} + \text{D}$, a three-body reaction, $\text{A} + \text{B} + \text{M} \rightarrow \text{C} + \text{M}$, or a photochemical reaction, $\text{A} + \text{h}\nu \rightarrow \text{C} + \text{D}$, is given by:

$$r_{d,p} = \frac{k_{2b,3b,ph} \times \prod_i n_i}{\sum_{d,p} k_{2b,3b,ph} \times \prod_i n_i} \times 100\% \quad (4)$$

Here, $k_{2b,3b,ph}$ represents the rate coefficient of the two-body (2b), three-body (3b), or photochemical (ph) reaction under consideration, and n_i denotes the number density of the i^{th} reactant in that reaction. The product is taken over all reactants, and the summation is performed over all reactions that destroy or produce the species of interest. In terms of volume mixing ratios, the number density is expressed as $n_i = (\text{VMR})_i \times n_{\text{gas}}$. The total gas number density n_{gas} for a given atmospheric layer is determined from the ideal gas law: $n_{\text{gas}} = p/(k_B T)$, where p is the pressure, k_B is the Boltzmann constant, and T is the temperature of the layer.

To assess the dominant formation and destruction pathways of the major contributors to the observed reflected and emitted fluxes on modern Earth-like exoplanets, we identify reactions contributing more than 10% to the total production or destruction of each species at any altitude. These key reactions and their relative contributions are summarized in Table 7 for both HWO and LIFE. For each molecule, the “% contribution” column lists the local maxima and minima of each reaction’s fractional contribution to its total production or destruction rate, with the corresponding altitudes shown in the adjacent column.

Note that the percentages do not sum to 100%, since each value corresponds to a local maximum or minimum specific to an individual reaction and does not represent a complete partitioning of the destruction/production pathways at a given altitude. For example, the first line in the table represents a major destruction pathway of O_3 . As altitude increases from 0 km to 4.5 km, the percentage contribution of this reaction to the total O_3 destruction decreases from 73% to 40.15%. Between 4.5 km and 31.32 km, the contribution increases again from 40.15% to a maximum of 47.41%, before declining to 10.36%.

In some cases, such as the production of N_2O via NH_2 and NO_2 , a constant dominance of nearly 100% persists from the surface up to 30 km, after which the contribution begins to decline. For all reactions, we report contributions down to $\sim 10\%$. If the percentage rises above $\sim 10\%$ again at higher altitudes, those values are shown as well.

At any given altitude, the total percentage contribution of all destruction as well as production reactions of any molecule (e.g., O_3) will sum to 100%. We have not aligned percentage values across the same altitudes for all molecules, since a given altitude may not correspond to a local maximum or minimum for every species.

Table 7. Major chemical reaction pathways and their contributions to the atmosphere of modern Earth-like exoplanets.

Species	Reaction	Reaction Type	% Contribution	Altitude (km)
O_3	$\text{O}_3 \rightarrow \text{O}_2 + \text{O}^a$	Photo-dissociation	73 – 40.15 – 47.41 – 10.36	0 – 4.5 – 31.32 – 79.11
	$\text{NO} + \text{O}_3 \rightarrow \text{NO}_2 + \text{O}_2^a$	Two-body	14.68 – 76 – 5.26	0 – 8.76 – 35.19
	$\text{O}_3 \rightarrow \text{O}_2 + \text{O}({}^1\text{D})^a$	Photo-dissociation	11.68 – 10.13 11.11 – 85.33 – 25.81 – 31.25	0 – 3.47 16.06 – 58.61 – 89.85 – 112.9
O_2	$\text{O}_3 + \text{H} \rightarrow \text{OH} + \text{O}_2^a$	Two-body	11.57 – 69.58 – 62.9	75.75 – 89.85 – 112.9
	$\text{O} + \text{O}_2 + \text{M} \rightarrow \text{O}_3 + \text{M}^b$	Three-body	100	0 – 112.9
O_2	$\text{O} + \text{O}_2 + \text{M} \rightarrow \text{O}_3 + \text{M}^a$	Three-body	96.08 – 98.8 – 15.32 – 63.03 – 13	0 – 8.76 – 81.59 – 90.68 – 100
	$\text{O}({}^1\text{D}) + \text{O}_2 \rightarrow \text{O} + \text{O}_2^a$	Two-body	10.25 – 16.37 – 10.06	32.28 – 52.19 – 74.03
	$\text{O}_2 \rightarrow \text{O} + \text{O}^a$	Photo-dissociation	10.1 – 41.85 – 24.94 – 41.82 – 24.7	70.47 – 81.59 – 89.02 – 98.28 – 112.9
	$\text{H} + \text{O}_2 + \text{M} \rightarrow \text{HO}_2 + \text{M}^a$	Three-body	10.63 – 38.82 – 13.34	72.27 – 82.41 – 86.54
	$\text{O}_2 \rightarrow \text{O} + \text{O}({}^1\text{D})^a$	Photo-dissociation	10.78 – 70.06	94.87 – 112.9
	$\text{O}_3 \rightarrow \text{O}_2 + \text{O}^b$	Photo-dissociation	70.95 – 18.51 – 58.01 – 10.08	0 – 8.76 – 23.94 – 67.68
	$\text{NO} + \text{O}_3 \rightarrow \text{NO}_2 + \text{O}_2^b$	Two-body	14.27 – 75.72 – 11.04	0 – 8.76 – 25.75
	$\text{O}_3 \rightarrow \text{O}_2 + \text{O}({}^1\text{D})^b$	Photo-dissociation	11.35 – 10.72 10.83 – 69.75 – 12.47 12.88 – 10.1	0 – 2.33 16.06 – 52.19 – 79.94 90.68 – 95.72
	$\text{O}({}^1\text{D}) + \text{O}_2 \rightarrow \text{O} + \text{O}_2^b$	Two-body	10.27 – 16.42 – 10.07	32.28 – 52.19 – 74.03

Table 7 *continued*

Table 7 (continued)

Species	Reaction	Reaction Type	% Contribution	Altitude (km)
	$O + OH \rightarrow O_2 + H^b$	Two-body	10.05 – 70.78	100.02 – 112.9
	$O + HO_2 \rightarrow OH + O_2^b$	Two-body	10.12 – 46.12 – 11.07	70.47 – 82.41 – 101.78
	$O_3 + H \rightarrow OH + O_2^b$	Two-body	10.59 – 37.14 – 11.05	72.27 – 81.59 – 86.54
	$O + O + M \rightarrow O_2 + M^b$	Three-body	11.29 – 34.89 – 10.08	83.23 – 89.85 – 101.78
			10.13 – 58.9 – 26.14	91.51 – 103.57 – 112.9
H ₂ O	$O(^1D) + H_2O \rightarrow OH + OH^a$	Two-body	97.38 – 82.88 – 85.12 – 12.88	0 – 35.19 – 47.83 – 73.16
	$H_2O \rightarrow H + OH^a$	Photo-dissociation	10.11 – 17.08 – 14.84 – 88.42 – 85.53	23.94 – 35.19 – 47.83 – 101.78 – 112.9
	$HNO_3 + OH \rightarrow NO_3 + H_2O^b$	Two-body	46.4 – 91.34 – 73.52 – 85.95 – 11.27	0 – 16.06 – 23.04 – 28.5 – 40.28
	$OH + CH_4 \rightarrow H_2O + CH_3^b$	Two-body	17.97 – 10.8	0 – 7.76
			10.3 – 13.1 – 10.21	35.19 – 39.24 – 43.48
	$NO + NH_2 \rightarrow N_2 + H_2O^b$	Two-body	11.03 – 13 – 10.45	20.39 – 22.15 – 23.94
	$OH + HO_2 \rightarrow H_2O + O_2^b$	Two-body	11.67 – 96.42 – 67.86 – 13.94	33.24 – 65.75 – 80.76 – 84.06
	$HO_2 + H \rightarrow O + H_2O^b$	Two-body	11.09 – 30.13 – 99.35	76.6 – 80.76 – 111.97
CO ₂	$O(^1D) + CO_2 \rightarrow O + CO_2^a$	Two-body	100 – 11.09	0 – 91.51
			10.57 – 14.59	109.1 – 112.9
	$CO_2 \rightarrow CO + O(^1D)^a$	Photo-dissociation	12.02 – 49.5 – 10.5	77.44 – 82.41 – 90.68
	$N + CO_2 \rightarrow CO + NO^a$	Two-body	16.97 – 92.28 – 65.49	86.54 – 97.42 – 112.9
	$OH + CO \rightarrow H + CO_2^b$	Two-body	95.48 – 12.5	0 – 15.19
			10.05 – 89.23 – 10.55	70.47 – 81.59 – 88.19
	$O(^1D) + CO_2 \rightarrow O + CO_2^b$	Two-body	16.4 – 99.83 – 10.52 – 79.8 – 10.08	2.33 – 51.1 – 81.59 – 89.02 – 109.1
	$O(^1D) + CO \rightarrow CO_2^b$	Two-body	12.2 – 91.66	89.02 – 112.9
CH ₄	$OH + CH_4 \rightarrow H_2O + CH_3^a$	Two-body	99.98 – 43.97 – 80.43 – 12.25	0 – 23.94 – 40.28 – 71.38
	$O(^1D) + CH_4 \rightarrow OH + CH_3^a$	Two-body	13.2 – 52.51 – 18.34 – 54.26 – 13.7	16.06 – 23.94 – 40.28 – 67.68 – 73.16
	$CH_4 \rightarrow ^1CH_2 + H_2^a$	Photo-dissociation	13.69 – 47.44 – 44.25	70.47 – 82.41 – 111.97
	$CH_4 \rightarrow CH_3 + H^a$	Photo-dissociation	12.02 – 41.64 – 36.39	70.47 – 83.23 – 112.9
	$CH_3 + HO_2 \rightarrow CH_4 + O_2^b$	Two-body	99.99 – 10.66 – 99.65 – 11.45	0 – 13.42 – 34.21 – 83.23
	$CH_3 + HNO \rightarrow NO + CH_4^b$	Two-body	12.44 – 87.85 – 10.47	5.66 – 12.52 – 22.15
	$CH_3CHO \rightarrow CH_4 + CO^b$	Photo-dissociation	12.96 – 16.43	17.78 – 19.51
	$H + CH_3 + M \rightarrow CH_4 + M^b$	Three-body	11.69 – 99.48 – 95.29 – 96.96	65.75 – 88.19 – 103.57 – 112.9
N ₂ O	$O(^1D) + N_2O \rightarrow NO + NO^a$	Two-body	62.1 – 10.52	0 – 20.39
	$O(^1D) + N_2O \rightarrow N_2 + O_2^a$	Two-body	37.9 – 12.65	0 – 17.78
	$N_2O \rightarrow N_2 + O(^1D)^a$	Photo-dissociation	15.65 – 94.15 – 92.39 – 99.84 – 91.73	14.31 – 30.38 – 48.92 – 81.59 – 112.9
	$NH_2 + NO_2 \rightarrow N_2O + H_2O^b$	Two-body	100	0 – 30.38
			100 – 10.62	30.38 – 37.19
	$N + NO_2 \rightarrow N_2O + O^b$	Two-body	42.8 – 100 – 99.99	36.19 – 63.77 – 112.9

Notes. ^a Destruction reaction; ^b Production reaction.

O_3 and H_2O are the primary species responsible for several spectral features observed at different wavelengths, including major dips at 0.3 μm , 1.3–1.5 μm , and 1.8–2 μm in the HWO reflection spectra (see Figure 4). As expected, in the lower stratosphere, ozone absorbs incoming UV photons, causing the temperature of this layer to rise. In these layers, ozone is produced from O_2 through reactions involving a third body. Throughout the upper atmosphere (above 35 km), most O_3 destruction occurs via photochemical dissociation, while its production remains dominated by a three-body mediated reaction (contributing 100%). In the lower atmosphere (0–20 km), its major destruction pathways involve photochemistry and two-body reactions.

H_2O is the most prominent greenhouse gas in Earth's atmosphere. From the surface to the lifting condensation level (LCL, ~ 2 km, where water begins to condense), the abundance of water vapor is maintained in balance between its production and destruction rates. However, as the rising air parcel cools, its capacity to hold water vapor decreases, leading to a reduction in its abundance. Beyond the LCL, condensation occurs, resulting in a further decrease in water vapor concentration up to the tropopause, beyond which transport is primarily mediated by diffusive mixing. This decline in H_2O abundance is further influenced by the two-body reaction involving $O(^1D)$ and OH , which contributes more than 90% for altitudes up to ~ 20 km. In the stratosphere and above, water vapor abundance remains relatively constant, as its initial concentration is primarily balanced by destruction processes involving $O(^1D)$ and UV photolysis (which produces H and OH radicals), as well as by its formation through the reaction of HNO_3 with OH . Beyond 80 km, H_2O abundance falls below 10^{-7} , rendering its chemistry insignificant.

By fixing the CO_2 abundance at 400 ppm, as done by Tsai et al. (2021), we observe no significant change in its concentration across altitudes up to ~ 80 km, beyond which it undergoes destruction due to photochemical dissociation and reactions with atomic nitrogen. The abundance of CO_2 , primarily due to the major flux contribution from the lower layers of the atmosphere, remains largely unaffected by atmospheric chemistry. In these layers, CO_2 is primarily produced and destroyed through reactions with excited oxygen ($O(^1D)$). The initial concentration of CO_2 at altitudes other than the surface remains consistent due to a near balance between its formation and destruction rates. However, destruction eventually outpaces production, which is compensated by the pre-existing OH and CO species, maintaining equilibrium.

O_2 is a major photochemical product in Earth's modern atmosphere. Its abundance remains relatively constant up to altitudes of ~ 85 km. Its major altitude-dependent formation and destruction reactions are detailed in Table 7. Regardless of its initial boundary conditions, O_2 remains well-mixed throughout the atmosphere up to about 80–85 km.

In the troposphere, methane reacts with OH to produce H_2O , with reaction rates for this process slightly exceeding those contributing to methane formation, as shown in Table 7. Consequently, its abundance gradually decreases with altitude up to approximately 80 km, beyond which it declines more rapidly due to photochemical destruction.

N_2O remains well-mixed in the troposphere, where the atmosphere is nearly devoid of N_2O sinks (Tsai et al. 2021). The limited chemical reactions governing its production and destruction are detailed in Table 7. In the lower atmosphere (up to approximately 15 km), N_2O is primarily destroyed by $O(^1D)$. In the stratosphere, it is predominantly removed through photodissociation and is not effectively replenished by two-body reactions.

3.2. Reflection Spectra using PSG: Observables for HWO

In this section, we present the reflection spectra obtained from PSG, which is expected as a synthetic observation from HWO. As seen in Figure 4, the dips in the flux in the reflection spectra are primarily due to spectroscopically active molecules, namely H_2O , CO_2 , O_2 , CH_4 , and O_3 .

We have included Rayleigh scattering in our simulations. In Figure 4, which shows the flux, the sharp dip in the planet's flux as the wavelength decreases from 0.5 to 0.3 μm corresponds to Rayleigh scattering due to nitrogen and oxygen. We define the spectral regions as ultraviolet (0.15–0.51 μm), visible (0.51–1.0 μm), and near-infrared (1.0–2.0 μm). The sharp transitions at 0.51 μm and 1.0 μm shows detector-specific sensitivity regions and to reflect the varying resolving power relevant to HWO. In the reflection spectrum, O_2 exhibits distinct absorption features that can be used to infer its presence and concentration. Key features occur at wavelengths around 0.69 μm and 0.76 μm , corresponding to the O_2 B-band and A-band, respectively. The A-band at 0.76 μm is particularly stronger than the B-band. Additionally, there is a very weak absorption feature at around 1.27 μm , which is not distinguishable in Figure 4 at low resolution, whereas features at other wavelengths remain prominent. Similarly, CH_4 has several spectral features, including relatively weak ones in the near-infrared (at 1.65 μm), which can be detected at a resolution of 70.

O_3 is photochemically produced from O_2 and, therefore, scales with atmospheric O_2 abundance. It exhibits strong spectral features across a range of wavelengths. Notable absorption occurs in the visible/near-infrared region (between 0.55 and 0.65 μm) and in the ultraviolet (~ 0.26 μm), both of which are evident in Figure 4. In the reflection spectrum shown in Figure 4, water vapor absorption features appear near 0.72 μm , 0.82 μm , 0.94 μm , 1.13 μm , 1.38 μm , and 1.87 μm . CO_2 exhibits weak features, particularly at 1.57 μm , which stands out in the reflection spectrum (refer to Figure 4).

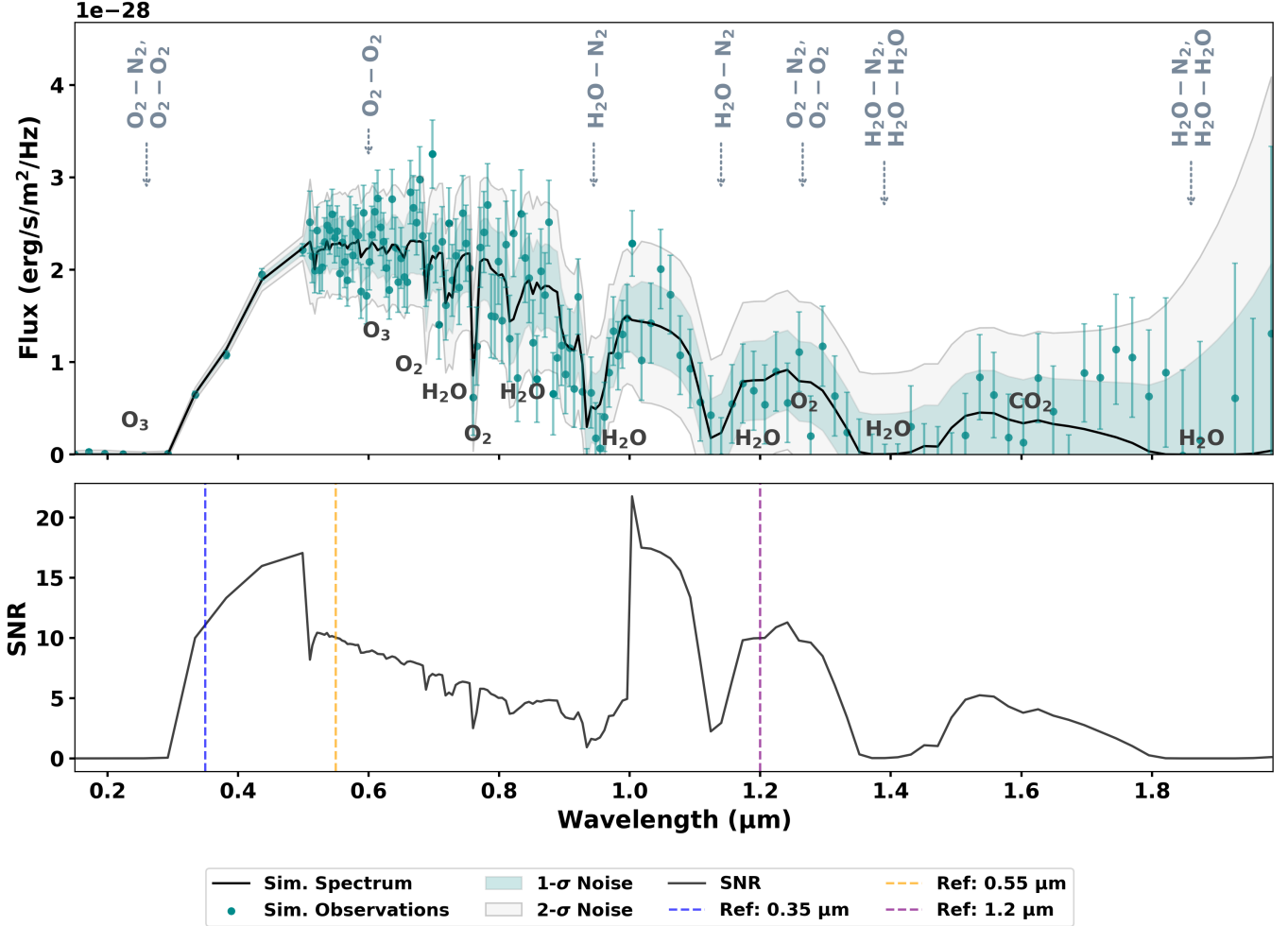


Figure 4. Top: simulated reflection spectra observation of modern Earth analog for the HWO mission concept. The simulated flux is considered for a planetary system at 10 pc distance. The wavelength is between 0.15 and 2 μm . The 1σ and 2σ error bars are represented with cyan and light grey shaded area with solid edges respectively. The black curve is the spectrum from PSG. The cyan scatter plot represents the simulated observation points with corresponding uncertainties. The simulated reflection spectra is considered at a phase angle of 77.8° . Molecular features are labeled in black, and CIA features are marked in grey; Bottom: the associated SNR vs wavelength for the reflection spectra. The SNR is assumed to be 10 at three reference wavelengths: 0.35 μm , 0.55 μm and 1.2 μm

The CIA features identified in the spectra include H₂O - N₂, H₂O - H₂O, O₂ - N₂, and O₂ - O₂. The H₂O - N₂ CIA is observed at 0.94 μm , 1.12 μm , 1.37 μm , and 1.85 μm , aligning closely with the major water vapor features in the spectrum. While the H₂O - H₂O CIA primarily contributes to the prominent water features at 1.38 μm and 1.86 μm , its impact is limited compared to the stronger contributions from H₂O - N₂. Notably, the dips associated with H₂O - N₂ are stronger than those from the H₂O - H₂O CIA; however, both remain relatively minor compared to the broad and deep absorption bands of water at these wavelengths, which result from fundamental vibrational transitions. The O₂ - N₂ CIA feature appears at 0.22 μm in the UV region and enhances the weak O₂ feature near 1.27 μm , indicating the influence of nitrogen in the presence of oxygen. The O₂ - O₂ CIA contributes at similar wavelengths

(0.22 μm and $\sim 1.27 \mu\text{m}$), although its impact is less pronounced than that of O₂ - N₂. Additionally, O₂ - O₂ exhibits weaker features at 0.58 μm and 0.63 μm , where O₃ is the dominant contributor. This analysis demonstrates that while collision-induced absorption plays a role, the dominant spectral features are still the intrinsic absorptions of H₂O, O₂, and O₃.

We also present the expected noise levels in the spectra, with the corresponding SNR shown in the bottom plot of Figure 4, following the assumptions described in Section 2.4.1. The SNR subplot closely follows the spectral pattern observed in the flux ratio plot. This correlation arises because the SNR is calculated as the ratio of the flux ratio signal at each wavelength to the 1σ noise at that wavelength. Consequently, any dips in the flux ratio spectrum due to absorption features correspond to reductions in SNR at those wave-

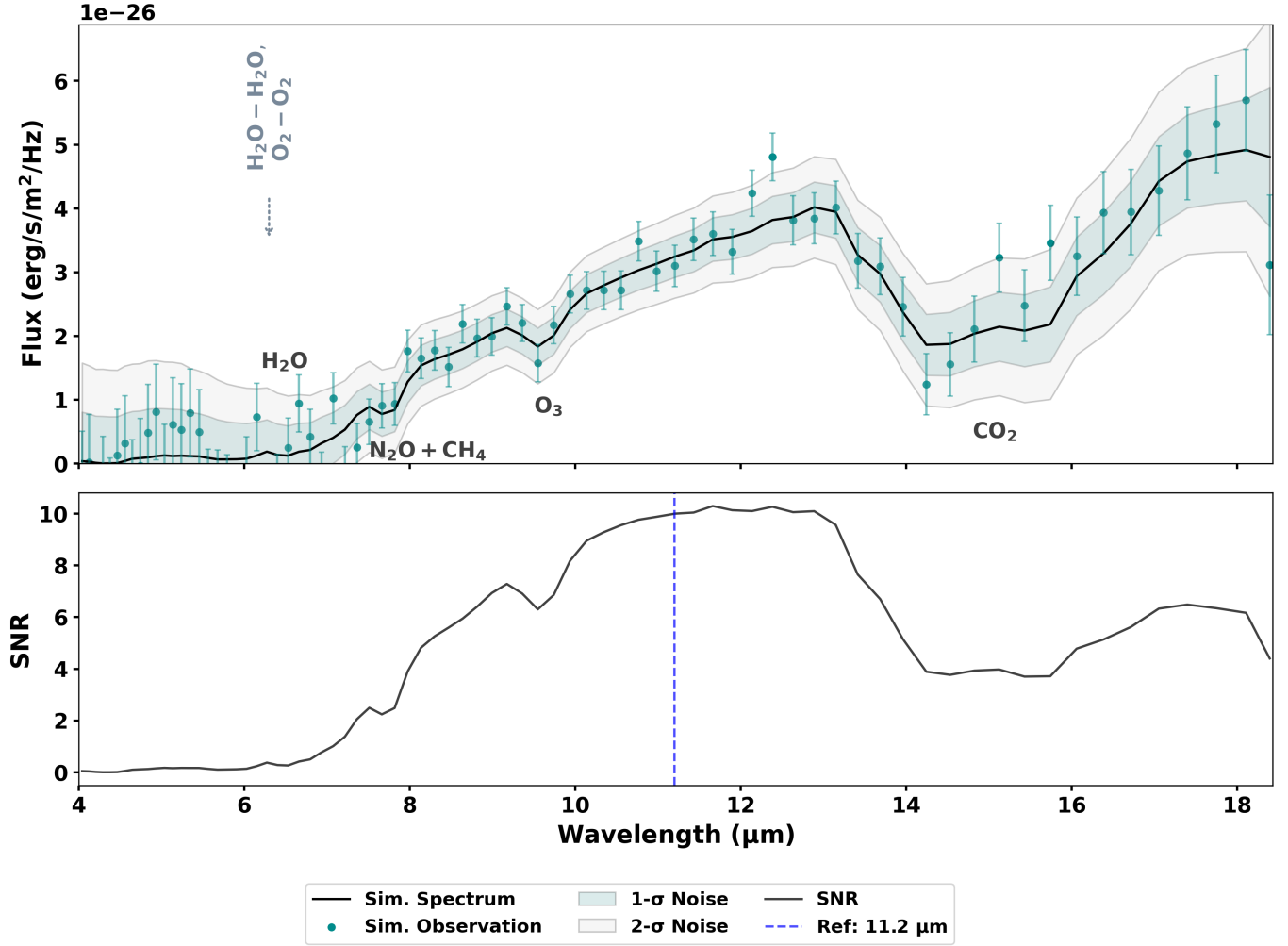


Figure 5. Top: simulated thermal emission spectra observation of modern Earth analog by the LIFE concept assuming a simplified noise. The simulated flux is considered for a planetary system at 10 pc distance. The wavelength is between 4 and 18.4 μm . The 1σ and 2σ error bars are represented with cyan and light grey shaded area with solid edges respectively. The black curve is the spectrum from PSG fed into LIFEsim to simulate the observation (cyan scatter plot) with error bars. The simulated reflection spectrum is considered at a phase angle of 77.8° . Molecular features are labeled in black, and CIA features are marked in grey; Bottom: the associated SNR vs wavelength for the thermal emission spectra. The SNR is assumed to be 10 at the reference wavelength $11.2\ \mu\text{m}$

lengths. The shaded regions in the main plot, representing 1σ and 2σ noise bounds, influence the depth of the SNR at specific wavelengths. Regions with broader noise bands indicate greater measurement uncertainty, leading to lower SNR values. This relationship between noise variations and SNR magnitude highlights how observational noise affects the detectability of spectral features, with the SNR plot emphasizing areas of higher and lower confidence in the signal based on the noise distribution.

The reflection spectra for all five Earth-like models, considering the boundary conditions discussed in Section 2.2.4, are shown in Figure 7 in Section 3.5.1. A detailed analysis of the visible features and the governing chemistry is provided in Sections 3.4 and 3.5.1.

3.3. Thermal Emission Spectra using PSG and LIFEsim: Observables for LIFE

In this section, we present the thermal emission spectra (refer to Figure 5) obtained from PSG, including the simulated synthetic observations expected from LIFE. As illustrated in the figure, the thermal emission spectra correspond to the presence of key spectrally active molecules such as H_2O , CO_2 , O_3 , CH_4 , and N_2O .

Additionally, we have calculated the expected noise levels in the spectra alongside the corresponding signal-to-noise ratio (SNR), both of which are illustrated in the bottom plot of Figure 5.

H_2O shows strong absorption features in the mid-infrared around $6.3\ \mu\text{m}$, which could be a signature of a moist atmosphere (Robinson & Reinhard 2019). CO_2 exhibits promi-

inent absorption features at 4.3 μm and around 15 μm . O_3 , a product of photochemical reactions involving oxygen, shows a distinct absorption feature at 9.6 μm . CH_4 reveals its presence through spectral features in the mid-infrared around 7.7 μm . Finally, N_2O displays a strong absorption feature around 7.7 μm . N_2O also has a feature at $\sim 16.9 \mu\text{m}$, but it is not distinguishable as it is masked by overlapping spectral lines of CO_2 and H_2O in the same region.

We observe that the only collision-induced absorption (CIA) features contributing to the spectra are $\text{H}_2\text{O} - \text{H}_2\text{O}$ and $\text{O}_2 - \text{O}_2$. These features are located in a region dominated by a very strong H_2O absorption feature, making their contributions comparatively minor relative to the broad, deep, and continuous H_2O features. The $\text{O}_2 - \text{O}_2$ CIA is a small feature, contributing from 5.9 μm to 7 μm , with a peak at 6.44 μm . In contrast, the $\text{H}_2\text{O} - \text{H}_2\text{O}$ CIA has a much broader shape, with a base spanning from 5 μm to 8 μm and a peak around 6.17 μm .

The noise levels for the thermal emission spectra, along with the corresponding SNR, are also presented in the bottom subplot of Figure 5. These values were calculated following the description in Section 2.4.2. The thermal emission spectra are simulated over the wavelength range of 4 to 18.5 μm with a constant resolution of $R = 50$, unlike HWO spectra. The SNR plot closely follows the features present in the spectrum. This means that as specific emission features appear in the spectrum, corresponding variations in the SNR are observed, with the SNR value for each feature shaped by the noise level around that wavelength. The consistent resolution allows for a clear representation of these features, indicating that the detectability of the signal is directly influenced by the spectral characteristics within this range.

The thermal emission spectra for all five Earth-like models, considering the varying boundary conditions discussed in Section 2.2.4, are shown in Figure 8 in Section 3.5.2. An analysis of the observable features and the underlying chemistry is provided in Sections 3.4 and 3.5.2.

3.4. Atmospheric Chemistry for Earth-like Models with Varying Boundary Conditions

In this section, we present the Earth-like model simulations (as described in Section 2.2.4) considering variations in the bottom boundary conditions that reflect biological and geological processes. We discuss their chemistry and in the following section, assess how they influence the atmospheric spectra. A summary of the models can be found in Table 3.

The mixing ratio profiles for all the models are shown in Figure 6. In the figure, we notice that for models where we have a bottom boundary, H_2O abundance decreases up to $\sim 20 \text{ km}$ when we fix its surface mixing ratio. Beyond which H_2O VMR is very well mixed until around 80 km and then further decreases due to photochemical reactions.

However, when bottom boundary conditions are not applied and H_2O mixing ratio is not fixed at the surface, it remains well-mixed from the surface level without showing any significant deviations below 20 km. For CH_4 , the VMR gets significantly affected by the boundary conditions throughout the atmosphere. In the absence of bottom boundary conditions, CH_4 shows major VMR change $\sim 10^{-22} - 10^{-30}$ from 10^{-6} (when bottom boundary remains present), whereas CO decreases by four orders of magnitude, as expected, due to the absence of its surface flux. CO_2 , however, remains abundant at 400 ppm even when there is neither its source nor its sink, along with no fixed surface abundance. Nitrogen-bearing species such as N_2O in the absence of tropospheric sinks keep on building up in the atmosphere due to surface sources up to a VMR of $\sim 10^{-6}$. However, its VMR falls due to photodissociation in the stratosphere and beyond. In the absence of N_2O bottom boundary, its VMR does not go above $\sim 10^{-12}$. In all these models, O_2 remains highly abundant.

In HWO spectra for M1 and M3 as shown in Figure 7 in Section 3.5.1, H_2O is seen to be absent at $\sim 0.9 \mu\text{m}$, 1.1 μm , and 1.4 μm compared to the rest of the cases. The reactions responsible for H_2O consumption are as follows: (i) $\text{SO}_3 + \text{H}_2\text{O} \rightarrow \text{H}_2\text{SO}_4$ contributing 59% – 94% for upto 4.5 km and <29% beyond, and (ii) $\text{O}(\text{¹D}) + \text{H}_2\text{O} \rightarrow \text{OH} + \text{OH}$ contributing upto 42% within 4.5 km, till 100% for upto $\sim 21 \text{ km}$. In addition to the chemical reactions that continuously produce H_2O , the supply of a fixed H_2O abundance at the surface (see Table 3) is necessitated by the appearance of H_2O feature in the HWO spectra. When the surface abundance of H_2O is fixed, the aforementioned chemical reactions will be unable to deplete the H_2O abundance near the surface as they do in the upper atmosphere (above $\sim 20 \text{ km}$). At $\sim 1.55 \mu\text{m}$ and $\sim 1.96 \mu\text{m}$ in models M1 and M3, prominent CO_2 features are present because of the absence of H_2O (more prominent in M3) and contribute similar to Table 7. For M3, upto 6.6 km, a reaction involving singlet oxygen contributes to CO_2 formation from 82 – 91% ($\sim 100\%$ for M1), while the same reaction destroys CO_2 ($\sim 100\%$) and the net CO_2 abundance does not change from the initial atmospheric abundance due to this dominant reaction. This is in contrast to the atmosphere having fixed boundary conditions (Table 7) where the formation reaction of CO_2 at lower atmosphere is dominated by the reaction involving OH and CO . In M3, the reactants OH and CO contribute upto a maximum of 18% near the surface (upto $\sim 5 \text{ km}$). This reaction plays an important role as the second dominating reaction when the major reaction involving $\text{O}(\text{¹D})$ almost nullifies the production of CO_2 with its destruction. So, the abundance of CO from the surface emission also impacts the abundance of CO_2 at any particular atmospheric layer. In the absence of boundary (M1 and M2), the lack of CO source could di-

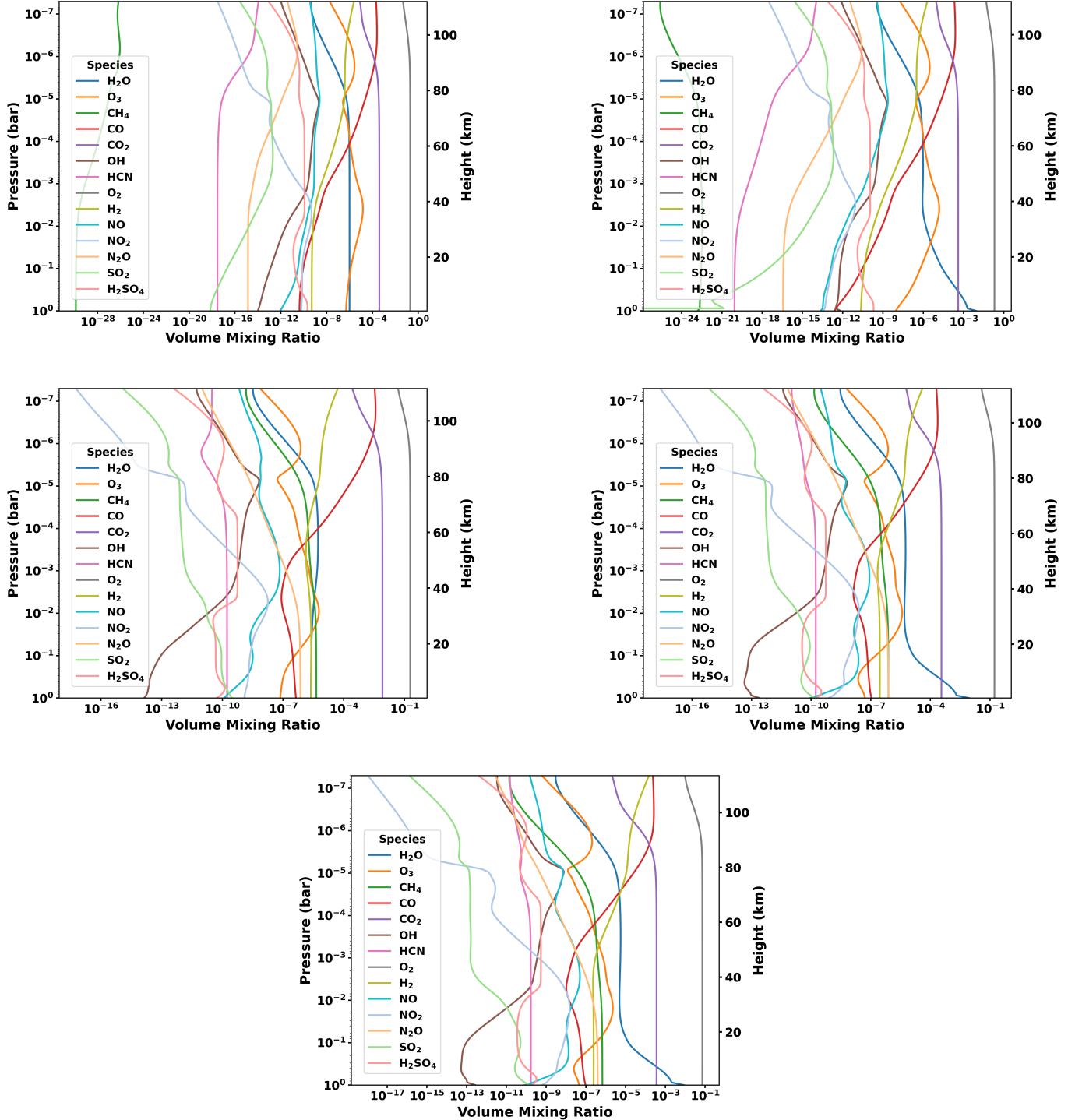


Figure 6. Comparison of mixing ratio profiles for Earth-like atmosphere by considering different boundary conditions (models M1 to M5) obtained from the kinetics model VULCAN, based on the temperature-sampled average TP profile. The profiles are organized into three rows: the top row displays models M1 and M2, the middle row shows models M3 and M4, and the bottom row features model M5. Each subplot illustrates the mixing ratios for specific atmospheric molecules: H_2O , O_3 , CH_4 , CO , CO_2 , OH , HCN , O_2 , H_2 , NO , NO_2 , N_2O , SO_2 , H_2SO_4 , providing a comprehensive view of molecular distribution across the different models.

rectly deplete the CO_2 abundance while in the presence of boundary with CO_2 and O_2 fluxes (M4 and M5), CO_2 surface sink could decrease the CO_2 abundance. However, in

M3 there is a continuous CO flux as well as no CO_2 surface sink. Consequently, the abundance of CO_2 in M3 becomes slightly higher than the rest of the models. Above 90 km, the

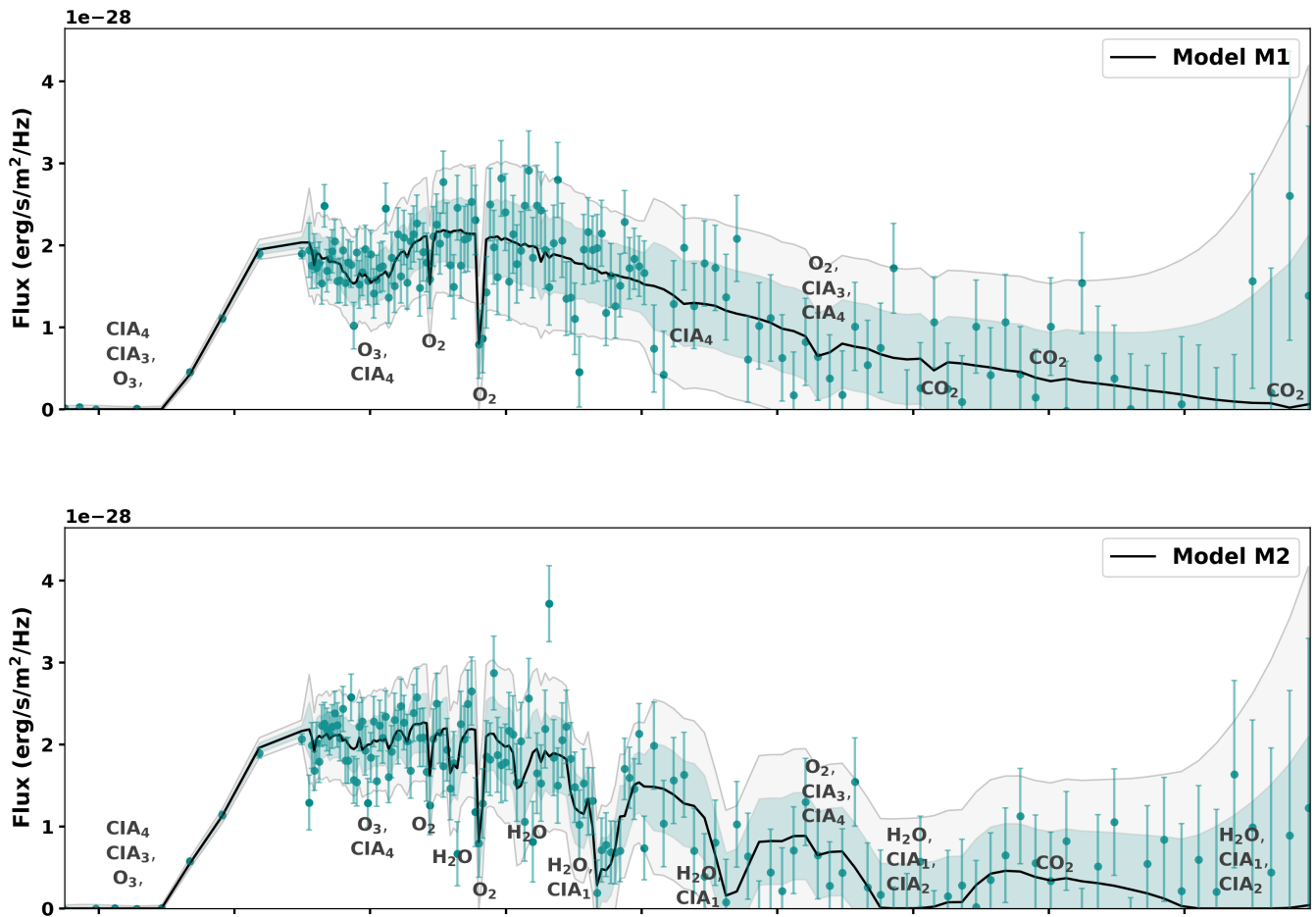
destruction reaction involving Nitrogen and the production reaction involving $O(^1D)$ and CO starts to exhibit major contribution, surpassing the contribution of the reaction (involving $O(^1D)$ and CO_2) which dominates the lower atmosphere.

For LIFE spectra in M1 and M2 (no boundary) as shown in Figure 8 in Section 3.5.2, CH_4 and N_2O at $7.9\ \mu m$ remain absent due to absence of their continuous surface flux. Whatever minor amount is produced gets consumed by the reactions as shown in Table 7. For N_2O , the first two destruction reactions of Table 7 for M1 and M2 remain 62% and 38% respectively across all layers upto 15 km, beyond which the destruction contribution starts to fall. In the absence of continuous surface emission flux, N_2O abundance diminishes to $\sim 10^{-16}$, which is orders of magnitude below detectable thresholds of LIFE. Similar to N_2O , the detectability of CH_4 also strongly depends on its surface emission flux. In the absence of continuous surface emission of CH_4 (M1 and M2), the initial abundance of CH_4 is majorly chemically destroyed by OH upto an altitude of 24.7 km, contributing $\sim 50 - 98\%$ ($\sim 97 - 100\%$ for M2), followed by the reac-

tion: $O(^1D) + CH_4 \rightarrow OH + CH_3$ contributing upto 47%. This reaction dominates above 24.7 km upto ~ 73 km, beyond which the CH_4 destruction is dominated by photodissociation to 1CH_2 (CH_2 singlet). In the LIFE spectra the presence of stronger CO_2 feature at $\sim 15\ \mu m$ (M3), as described previously, can be attributed to continuous CO flux and absence of CO_2 surface sink.

3.5. Simulated Reflection and Thermal Emission Spectra for the Earth-like Models

In this section, we present the simulated reflection and thermal emission spectra for all five models with varying boundary conditions (see Table 3 in Section 3.4). The reflection spectra are provided in Section 3.5.1, and the thermal emission spectra are shown in Section 3.5.2. We then discuss the molecular features that are evident in each spectrum. Furthermore, we consider how changes in boundary conditions impact the strength and presence of these spectral features.



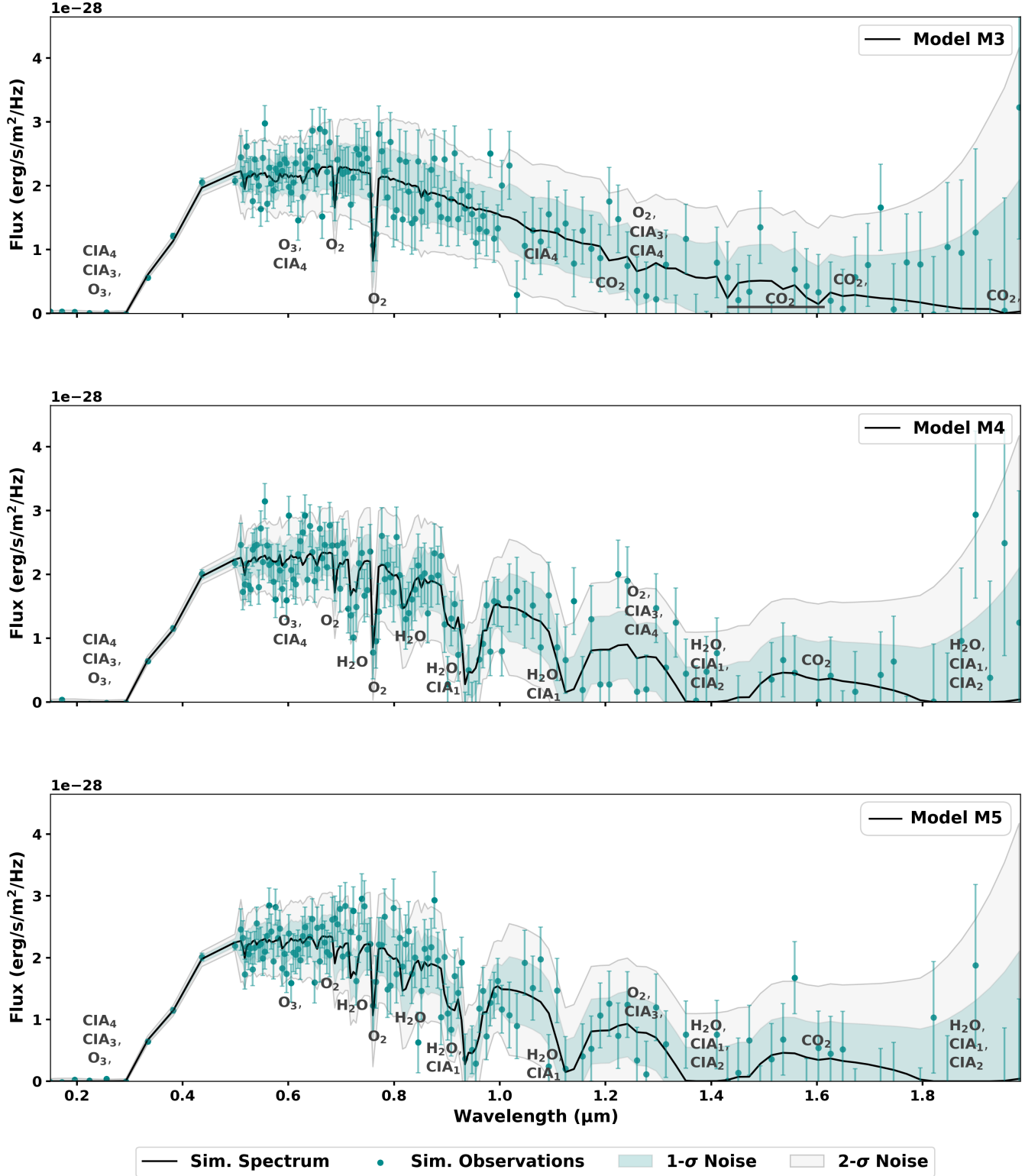


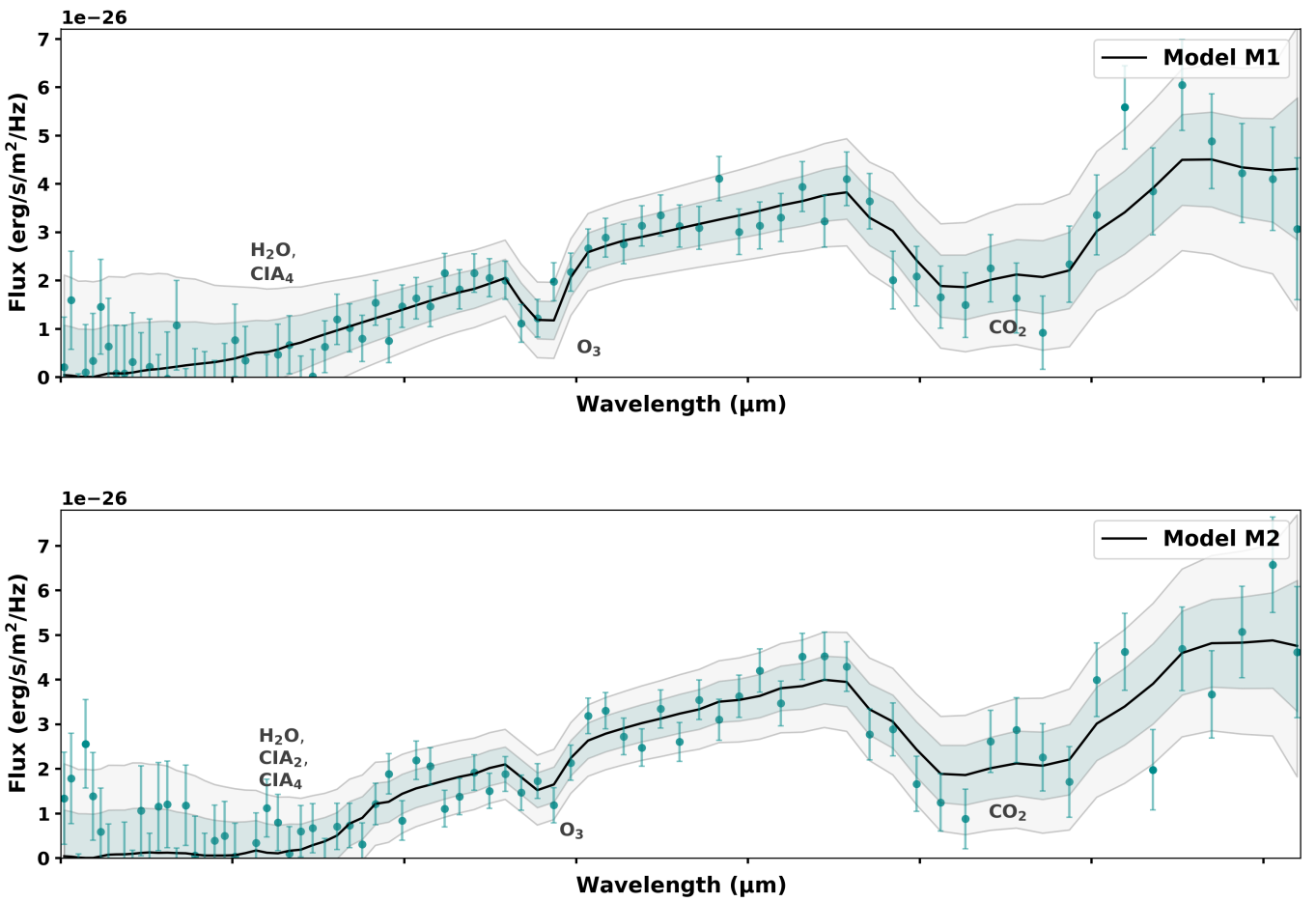
Figure 7. Simulated reflection spectra observation of Earth analog by considering different boundary conditions in the models M1 to M5 (top to bottom) for the HWO mission concept. The simulated fluxes are considered for a planetary system at 10 pc distance. The wavelength is between 0.15 and 2 μm . The 1σ and 2σ error bars are represented with cyan and light grey shaded area with solid edges respectively. The black curve is the spectrum from PSG. The cyan scatter plot represents the simulated observation points with corresponding uncertainties. The simulated reflection spectrum is considered at a phase angle of 77.8° . Here, CIA₁, CIA₂, CIA₃, and CIA₄ refer to H₂O – N₂, H₂O – H₂O, O₂ – N₂, and O₂ – O₂ CIAs respectively.

3.5.1. Reflection Spectra

For models M1 and M3 in the Figure 7, H_2O absorption features are absent around $\sim 0.9\text{ }\mu\text{m}$, $1.1\text{ }\mu\text{m}$, and $1.4\text{ }\mu\text{m}$ compared to the other models. This is due to the lower H_2O abundance, as shown in Figure 6. The absence of detectable H_2O in the spectrum is linked to the lack of a fixed H_2O surface abundance and the reactions responsible for H_2O consumption, as detailed in Section 3.4. Apart from this, other spectral features are still evident in these two models.

At $\sim 1.55\text{ }\mu\text{m}$ and $\sim 1.96\text{ }\mu\text{m}$, prominent CO_2 features are observed, particularly in the absence of H_2O , and are especially strong in model M3. In model M3, CH_4 is also clearly visible, unlike in model M1, because model M3 in-

cludes CH_4 under its default boundary conditions. In contrast, in model M2, even without default boundary conditions, the key features from the main model are still prominent. This is because molecules without defined fluxes or deposition velocities in the boundary file do not show features in this region (except for CH_4). CH_4 is not present in the boundary for model M2, and therefore, does not appear in its spectrum. However, O_2 and O_3 behave differently. Their abundances are high across all models, as shown in Figure 7, so their features are consistently visible. In the last two models, where we introduced a CO_2 boundary and varied the oxygen boundary while keeping other molecules fixed, we confirm that the abundances of O_2 , O_3 , and CO_2 are not significantly affected by these changes. As a result, their spectral features remain prominent in these models.



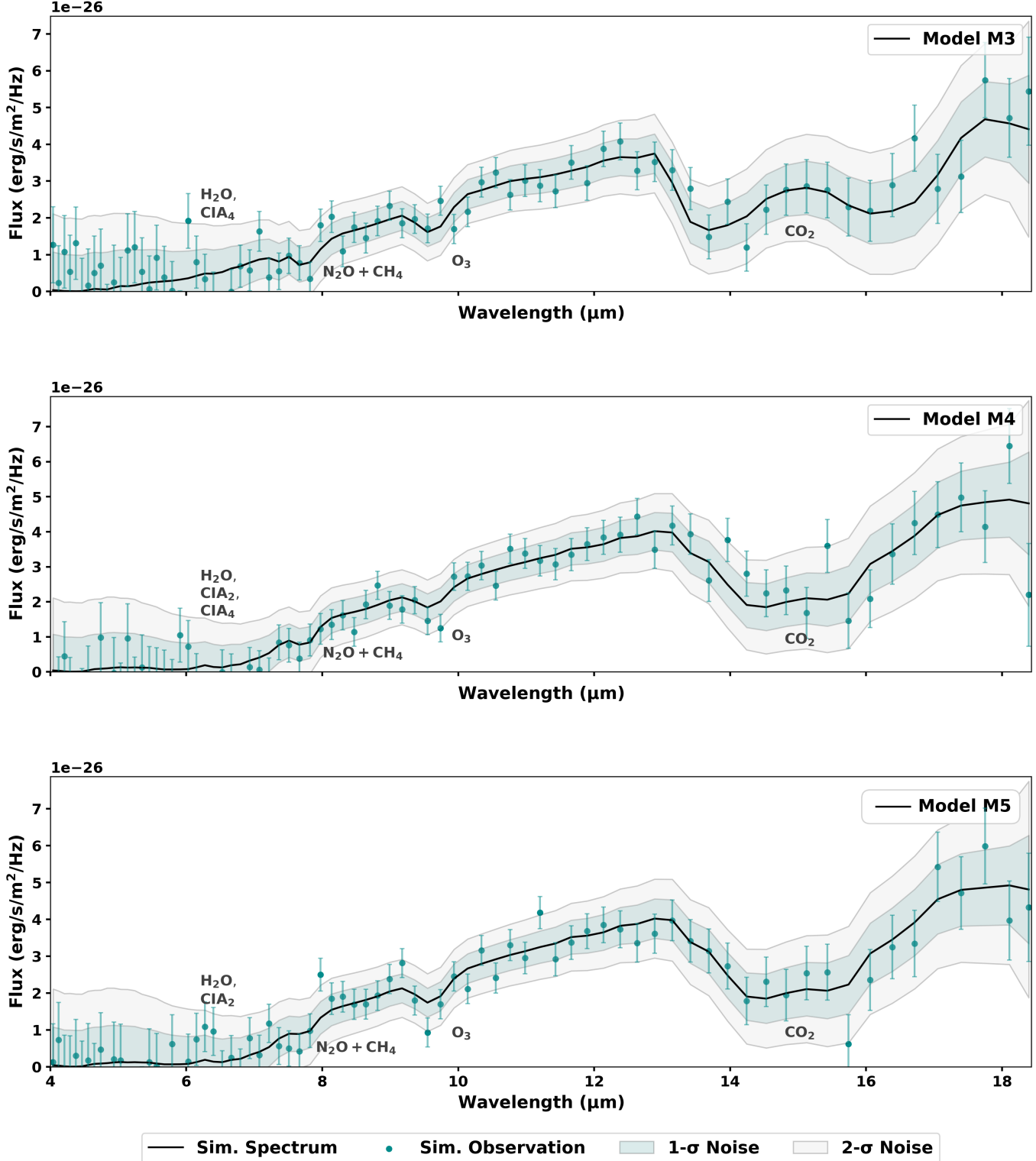


Figure 8. Simulated thermal emission observation of Earth analog by considering different boundary conditions in the models M1 to M5 (top to bottom) for LIFE. The simulated fluxes are considered for a planetary system at 10 pc distance. The wavelength is between 4 and 18.5 μm . The 1σ and 2σ error bars are represented with cyan and light grey shaded area with solid edges respectively. The black curve is the spectrum from PSG fed into LIFEsim. The cyan scatter plot represents the simulated observation points with corresponding uncertainties obtained from LIFEsim. The simulated thermal emission spectrum is considered at a phase angle of 77.8° . As like HWO spectra, here, CIA₂ and CIA₄ refer to H₂O – H₂O and O₂ – O₂ CIAs respectively.

We compare the CIA contribution in these models with those identified in our base spectra (see Figure 4), which include $\text{H}_2\text{O} - \text{N}_2$, $\text{H}_2\text{O} - \text{H}_2\text{O}$, $\text{O}_2 - \text{N}_2$, and $\text{O}_2 - \text{O}_2$. Notably, $\text{H}_2\text{O} - \text{N}_2$ and $\text{H}_2\text{O} - \text{H}_2\text{O}$ CIA are absent in models M1 and M3, attributed to the very low abundance of H_2O in these simulations. However, the CIA contributions from $\text{O}_2 - \text{N}_2$ and $\text{O}_2 - \text{O}_2$ are present in all the spectra across their respective wavelengths, as discussed in Section 3.2. This consistent presence is due to the robustness of O_2 detection, which is not significantly affected by boundary conditions. Additionally, we observe a faint feature of $\text{O}_2 - \text{O}_2$ CIA around $1.08 \mu\text{m}$ in models M1 and M3, which is otherwise obscured in the base model and other configurations due to overlapping water bands. Interestingly, $\text{O}_2 - \text{O}_2$ CIA is nearly absent in model M5. We note that O_2 VMR in this model is slightly below 0.1 (see Figure 7) as compared to other models suggesting that the VMR threshold for O_2 to contribute to this particular CIA feature is about 0.1.

3.5.2. Thermal Emission Spectra

For models M1 and M2 in Figure 8, the CH_4 and N_2O features around $7.9 \mu\text{m}$ are absent, as their abundances (shown in Figure 6) are too low to be detectable in the spectra. Any minor production is quickly consumed. Additionally, in model M1, the H_2O feature is too faint to be visible due to the lack of a specified fixed surface boundary for H_2O , resulting in very low production. Similarly, in model M3, the absence of a fixed bottom boundary for H_2O leads to its negligible presence in the spectra. However, in model M3, CH_4 and N_2O are observable in the spectra due to the default boundary conditions that allow for sufficient production of these molecules. In models M4 and M5, despite varying O_2 boundary conditions, all expected spectral features remain visible, confirming that O_2 and O_3 are not significantly affected by these boundary conditions. The strong CO_2 features present in all models are due to a balance between its production and destruction processes, keeping its levels consistent.

As discussed in Section 3.3, the only CIA features contributing to the thermal emission spectra are $\text{H}_2\text{O} - \text{H}_2\text{O}$ and $\text{O}_2 - \text{O}_2$. Among these, the contribution from $\text{H}_2\text{O} - \text{H}_2\text{O}$ is absent in models M1 and M3, as anticipated due to the very low abundance of H_2O in these configurations. In the other models, however, $\text{H}_2\text{O} - \text{H}_2\text{O}$ contributes. The $\text{O}_2 - \text{O}_2$ feature is present in all models, due to the high abundance of O_2 . However, as noted in Section 3.5.1, this CIA feature does not contribute in model M5, suggesting that the abundance of O_2 must exceed 0.1 for $\text{O}_2 - \text{O}_2$ CIA to play a role.

4. DISCUSSIONS

4.1. Inferences from previous studies

In this study, we conducted simulations for both HWO and LIFE, focusing on two distinct wavelength ranges corresponding to the reflected and thermal emission spectra of a modern Earth-like exoplanet. The HWO simulations covered wavelengths from 0.25 to $2 \mu\text{m}$, while the LIFE simulations spanned 4 to $18.5 \mu\text{m}$. Together, these missions can provide crucial insights into planetary atmospheres, their chemical compositions, and potential links to biosignature studies in exoplanetary environments.

The gases of primary interest for biosignature studies include O_2 , CH_4 , CO_2 , O_3 , and N_2O , among others (Schwieterman et al. 2018; Schwieterman & Leung 2024). On Earth, these gases are predominantly associated with biological activity, though not exclusively. Their detectability on exoplanets depends on several factors, including disequilibrium processes, atmospheric abundance, planetary distance, and observational constraints (Schwieterman et al. 2018). Some of these species can also be produced through abiotic processes, complicating their interpretation. Hence, identifying a molecule as a biosignature requires understanding its potential sources, encompassing both biotic and abiotic pathways.

For example, Meadows (2017); Meadows et al. (2018) have shown that O_2 may not be a reliable biosignature when considered in isolation. Abiotic mechanisms such as water photolysis followed by hydrogen escape, CO_2 photolysis in low non-condensable gas atmospheres, or pre-main-sequence water loss around M-dwarfs can all produce substantial amounts of O_2 and O_3 without biological input. Given the limited observational data currently available for exoplanets, interpretations often rely on models guided by terrestrial analogs.

In contrast, Krissansen-Totton et al. (2018) emphasized that the most reliable indicators of life may arise from atmospheric chemical disequilibrium, characterized by the co-existence of strongly oxidized and reduced species that are maintained far from thermodynamic equilibrium. Their analysis indicates that, for exoplanets, the simultaneous detection of abundant CH_4 and CO_2 , particularly in the absence of CO , would constitute a compelling biosignature, as maintaining high CH_4 levels abiotically is thermodynamically challenging. Such disequilibrium-based frameworks complement species-specific biosignature searches and can be directly tested with instruments like HWO and LIFE, which probe both CH_4 and CO_2 spectral features.

While our simulations demonstrate the detectability of certain species potentially linked to surface activity, whether biological or geological, they do not by themselves confirm the presence of biosignatures. Distinguishing between these possible origins remains a key challenge in interpreting future observations and highlights the importance of assessing

atmospheric redox disequilibria alongside broader planetary context.

4.2. Comparative detectability of key molecules with HWO and LIFE

As a metric for detecting molecular features of interest, we define the band-integrated signal-to-noise ratio (SNR) (see Section 2.4.3). Given that the exact noise characteristics of HWO and LIFE are not yet fully specified, the absolute detectability of molecular features cannot be determined with certainty. However, the band-integrated SNR values serve as a useful comparative metric, offering insights into the relative detectability of different molecules across various models. From the tabulated values of the band-integrated SNR for the Earth-like models presented in Table 8 for HWO, we infer that ozone has very high SNR values (greater than 10 in all cases), indicating that it is observable in all scenarios. In contrast, the SNR for oxygen ranges from around 3 to 5, i.e. below our marginal detectability range and therefore not detectable under the adopted instrument and noise criteria. H_2O falls into the potentially detectable regime (e.g., $\text{SNR} \sim 8\text{--}9$ in the $0.5\text{--}1 \mu\text{m}$ band) in the main model as well as in models 2, 4, and 5. However, for models 1 and 3, the SNR is too low due to the absence of water in the lower boundary (i.e., the lack of fixed surface humidity). CO_2 and CH_4 , on the other hand, exhibit very low SNR values, falling below the detection sensitivity threshold of HWO under the current setup. These molecules may require significantly longer integration times to be detectable. For the Earth-like models presented in Table 8 using LIFE and the proposed integration time, we find that H_2O , CO_2 , and O_3 have very high SNR values and would be clearly detectable in all considered models. However, CH_4 and N_2O present a more complex scenario. CH_4 is potentially observable in model 3, where it has a surface outgassing flux. It is not detectable when absent from the surface boundary conditions (models 1 and 2) or when H_2O is present at the boundary. The reason CH_4 is undetectable in the presence of H_2O at the lower boundary is that the H_2O absorption band in the $4\text{--}8 \mu\text{m}$ region is significantly stronger than the CH_4 absorption at around $7.5 \mu\text{m}$, effectively masking it. Finally, N_2O is detectable in the main model and in models 3, 4, and 5, where it is included in the boundary conditions. However, it remains undetectable in cases where it is absent from the boundary conditions.

For HWO, O_3 consistently shows the highest SNR across all models, with detectability several times greater than that of O_2 across the full wavelength range for the main model. H_2O shows potential detectability in models with a fixed surface abundance (for example, in the main model compared to Model 1, where the H_2O SNR decreases from 8.88 to 0.06). CH_4 remains undetectable in all HWO models, while CO_2 shows high detectability for LIFE.

For LIFE, H_2O is also generally the most detectable molecule, with SNR values exceeding 140 in the main model as well as in Models 4 and 5. CO_2 and O_3 remain readily observable but with lower relative SNR than H_2O . CH_4 and N_2O show greater variability: N_2O is detectable only when included through surface boundary conditions (e.g., $\text{SNR} \sim 10$ and 15 in Models 3 and 4, compared to 0 in Models 1 and 2), while CH_4 becomes marginally detectable ($\text{SNR} \sim 9$) in Model 3, where a surface outgassing flux is present.

These comparisons illustrate that the relative detectability of molecules depends strongly on both atmospheric composition and surface boundary conditions, highlighting which species are most likely to be observable under different planetary scenarios, independent of the precise instrument noise characteristics. This overlap in molecular detection between HWO and LIFE, with each instrument emphasizing different spectral regions and features, highlights the importance of studying these molecules collectively to obtain a more complete picture of the atmospheric composition of an Earth analog. By combining their strengths, we can better identify subtle atmospheric details and gain a deeper understanding of the planetary environment.

4.3. Inferences on detectability from photochemical modeling under varying boundary conditions

In the Earth-like photochemical models (see Section 3.4), where we varied boundary conditions to assess their impact on atmospheric spectra, the VMR profiles from VULCAN (Figure 6), the spectra (Figures 7 and 8), and the corresponding band-integrated SNRs reveal important details. Starting with H_2O , its abundance increases to highly detectable levels when its surface mixing ratio is fixed. Compared to models where the surface mixing ratio of water is not fixed, this deviation is most apparent below 20 km. Therefore, the low abundance of H_2O and its non-detectability in both reflection and thermal emission spectra can be attributed to the absence of a fixed surface abundance and to reactions that consume H_2O , as described in Section 3.4. In models lacking an H_2O feature in the HWO and LIFE spectra, even when bottom boundary fluxes of other molecules are included, the abundance of H_2O produced by atmospheric chemistry alone remains too low to be detectable. Thus, for an Earth-like detectable spectrum, the presence of H_2O likely indicates a fixed and relatively high surface water composition. When bottom boundary conditions are not considered, CH_4 also shows a major VMR shift (see Section 3.4) and is not abundant enough to be detectable in the thermal emission spectra. This finding suggests that a constant CH_4 outgassing flux and the absence of surface humidity are required to raise CH_4 levels to observable values. In the reflection spectra, CH_4 has a very low SNR and would be difficult to detect

Table 8. Band-integrated signal-to-noise ratios (SNRs) for different molecular features across various wavelength bands for HWO and LIFE simulations.

Models	HWO				LIFE	
	Mol. Feature	Band Int. SNR (intervals)			Mol. Feature	Band Int. SNR
		0.15–0.5	0.5–1	1–2		
Main Model	H ₂ O	1.39	8.88	5.62	H ₂ O	141.88
	CO ₂	1.39	1.02	0.35	CO ₂	52.76
	O ₃	17.29	3.29	0.3	O ₃	11.83
	O ₂	1.36	4.36	0.38	N ₂ O	15.04
	CH ₄	1.39	1.02	0.3	CH ₄	1.79
Model 1	H ₂ O	0	0.06	0.21	H ₂ O	4.14
	CO ₂	0.01	0.01	0.27	CO ₂	40.94
	O ₃	20.33	14.07	0	O ₃	42.03
	O ₂	1.87	4.33	0.59	N ₂ O	0
	CH ₄	0	0	0	CH ₄	0
Model 2	H ₂ O	0.04	8.48	4.58	H ₂ O	181.96
	CO ₂	0.01	0	0.11	CO ₂	53.28
	O ₃	18.22	6.46	0	O ₃	23.85
	O ₂	1.78	4.42	0.58	N ₂ O	0
	CH ₄	0	0	0	CH ₄	0
Model 3	H ₂ O	0	0.14	0.33	H ₂ O	6.51
	CO ₂	0.19	0.09	0.96	CO ₂	40.35
	O ₃	17.64	4.88	0	O ₃	17.56
	O ₂	1.72	4.4	0.56	N ₂ O	9.12
	CH ₄	0	0.02	0.13	CH ₄	9.13
Model 4	H ₂ O	0.04	8.56	4.59	H ₂ O	141.83
	CO ₂	0.01	0	0.11	CO ₂	54.07
	O ₃	17.27	2.87	0	O ₃	11.78
	O ₂	1.49	4.23	0.48	N ₂ O	15.21
	CH ₄	0	0	0.02	CH ₄	1.78
Model 5	H ₂ O	0.04	8.63	4.61	H ₂ O	144.92
	CO ₂	0.01	0	0.11	CO ₂	54.38
	O ₃	17.38	2.81	0	O ₃	14.8
	O ₂	0.65	3.31	0.22	N ₂ O	8.47
	CH ₄	0	0	0.01	CH ₄	2.04

with HWO under the initial conditions and proposed sensitivity considered here. In the absence of tropospheric sinks, nitrogen-bearing species such as N₂O can accumulate in the atmosphere from surface sources, reaching a VMR of approximately 10⁻⁶ (see Section 3.4), which is detectable in the thermal emission spectra. Therefore, detectable amounts of N₂O in the LIFE thermal emission spectra may indicate

continuous surface release, making it a strong biosignature candidate (Madhusudhan 2025). Thus, the spectral features of H₂O, CH₄, and N₂O become detectable only when there is a continuous surface supply or a stable surface abundance. Their absence in the spectra suggests that insufficient surface sources can significantly limit the detectability of these key molecules.

In all these models, O_3 , and CO_2 remain abundant and detectable in the LIFE spectra, even without a specific source, sink, or fixed surface mixing ratio. The constant CO_2 level at 400 ppm suggests that its major destroyer, $O(^1D)$, and its primary producers, CO and OH , are present in such small quantities that their reactions do not significantly alter the CO_2 abundance. Similarly, O_3 is very strongly detectable by HWO for all the models however O_2 is barely detectable by HWO in all the models even though it accumulates in the atmosphere regardless of boundary conditions and remains stable, unaffected by the chemistry of other molecules. So O_2 could be detectable with HWO with higher integration time than 100 hours. However the high O_2 abundance, in turn, supports elevated levels of O_3 , as ozone formation is largely driven by the availability of O_2 .

In our combined assessment of the base model and various Earth-like scenarios with modified boundary conditions, we find that the detectability of any spectral feature is primarily determined by its abundance, which depends on both local atmospheric chemistry and surface-atmosphere interactions. For example, the detectability of O_2 , O_3 , and CO_2 is largely maintained by atmospheric chemistry, irrespective of surface boundary conditions, whereas the detectability of H_2O , CH_4 , and N_2O strongly depends on their surface abundances. Thus, the observability of a molecular feature reflects the interplay between surface conditions and atmospheric chemistry. Furthermore, detecting a feature at a specific wavelength (e.g., CH_2 at $\sim 7.4 \mu m$) may indicate the absence of another molecule, pointing to different physical conditions near the surface (e.g., insufficient H_2O abundance). These characteristics of molecular signatures are crucial for interpreting future spectra from the HWO and LIFE missions.

In our simulations, we also identified wavelengths where CIA occurs alongside contributions from other molecules, as shown in Figures 4 and 7 for HWO, and Figures 5 and 8 for LIFE. We included all CIAs supported by PSG and discuss the specific CIAs that contribute to the spectra in Sections 3.2, 3.3, and Section 3.5. While the contributions of these CIAs are minimal, removing them does not significantly impact the overall spectral characteristics. Nonetheless, the presence of these subtle CIA features provides additional context for the spectral signatures and suggests possibilities for further exploration. CIAs not discussed in this paper have no measurable impact on the spectra.

4.4. Comparison with EPOXI observations of Earth analogs and potential limitations

We further compared our reflected light spectra from the base modern Earth main model without clouds to the cloud-free model of [Robinson & Salvador \(2023\)](#) and found good agreement. However, the best-fit Earth model of [Robinson & Salvador \(2023\)](#), which was used to reproduce the EPOXI

observations of Earth, included a mixed-phase cloud deck (50% liquid water and 50% ice) with blended optical properties, specifying the cloud-top pressure, thickness, and V-band optical depth. Since our PSG-generated spectra are limited to cloud-free atmospheres, we do not compare them directly with the EPOXI observations. Moreover, PSG's current one-dimensional cloud module does not support mixed-phase clouds within a single layer; only one cloud phase can be specified at a time, and optical properties cannot be blended within the same deck. While PSG can incorporate externally defined multi-layer or three-dimensional cloud fields, such an analysis to reproduce the EPOXI observations of Earth is beyond the scope of this paper.

4.5. Limitations and future work

Since the HWO mission concept and LIFE are still in the early stages of development, our simulations and assessments are based on the current understanding of their expected designs and capabilities. In this work, we are limited by the prescribed initial conditions and compositions used to simulate modern Earth-like environments. The photochemical model does not explicitly differentiate between biological and geological processes to robustly identify any species as a potential biosignature. Instead, it relies on boundary condition fluxes and deposition rates to represent them as indirect sources. Consequently, it remains challenging to designate any particular molecule as a confirmed biosignature. In the future, extending this study to develop a one-dimensional photochemical-ocean-ecosystem model would help distinguish the relative roles of biotic and abiotic processes in the origin of these molecules.

5. CONCLUSIONS

In this study, we perform forward modeling of several Earth analogs using temperature-pressure (T-P) profiles derived from a Numerical Weather Prediction model coupled with a one-dimensional chemical kinetics model to generate both reflection and thermal emission spectra and to evaluate their detectability under different surface conditions, which may be indirectly linked to possible biological or geological activity. Specifically, our work predicts the spectra expected for Earth analogs when observed with future facilities such as HWO and LIFE. We further assess the scientific potential of these two mission concepts for the Earth-like scenarios considered here by using the band-integrated SNR, which we classify as follows: detectable if $SNR \geq 10$, potentially detectable if $5 \leq SNR < 10$, and not detectable if $SNR < 5$. Our key findings and conclusions are summarized below:

- O_3 is detectable with both HWO and LIFE regardless of its surface boundary conditions for the Earth analogs, since its atmospheric abundance is primarily

governed by photochemical processes. Its spectral signature remains robust even in the absence of direct surface sources or sinks.

- For modern Earth analogs shaped by biological and geological processes, we find that the band-integrated SNR for O_2 in the 0.5–1.0 μm wavelength range reaches slightly above 4 for HWO. In contrast, O_2 features in the 0.15–0.5 μm and 1–2 μm ranges remain consistently weaker, even when surface emission or deposition processes are included for other Earth analogs. This indicates that the 0.5–1.0 μm band provides the most promising window for future O_2 detection, particularly with longer integration times.
- For all Earth analog cases considered in this study, continuous surface outgassing of CH_4 driven by biological and geological activity, together with low surface humidity, is required for its potential detectability with LIFE. Spectral resolutions higher than 50 can be expected to further improve its detectability.
- Similar to CH_4 , N_2O becomes potentially detectable in the modeled Earth analogs by LIFE only when it is continuously supplied through surface emission fluxes associated with biological and geological activity.
- The band-integrated SNR for H_2O with both HWO and LIFE increases when a fixed specific humidity is maintained at the surface, making H_2O potentially detectable with HWO and detectable with LIFE. This underscores the importance of surface boundary conditions for water vapor detectability.
- CO_2 is consistently detectable for LIFE across nearly all Earth analogs considered here, indicating that it does not require continuous surface emission or deposition for detection and remains observable regardless of surface dynamics. However, HWO cannot detect CO_2 in the same modeled Earth analogs, likely due to the weaker absorption features within its accessible wavelength range.
- Observations in the UV/VIS/NIR range with HWO provide key information about atmospheric composition and surface properties. However, for the modeled Earth analogs considered here, the band-integrated SNR indicates that neither CH_4 nor CO_2 is detectable with HWO under our assumed instrument and noise conditions.
- Each wavelength range (UV/VIS/NIR for HWO and mid-IR for LIFE) provides unique insights along with specific observational challenges. However, combining data from these spectral regions yields a more comprehensive understanding of exoplanetary atmospheres

and enhances our ability to identify Exo-Earths influenced by biological and geological processes. Such a multi-wavelength approach also improves our understanding of their role in the broader quest to search for habitable Exo-Earths.

- The methodology and results presented here focus on the UV/VIS/NIR and mid-IR regions, in line with future mission concepts such as HWO and LIFE. However, our work and findings would also be helpful for any future missions aiming to characterize Earth-like worlds using reflected light and thermal emission spectra in these spectral regions.

6. ACKNOWLEDGMENTS

L.M. sincerely thanks Dr. Ravi Kumar Kopparapu (NASA GSFC) for insightful discussions on the photochemistry of Earth analogs and on noise simulations for the Habitable Worlds Observatory (HWO). We are grateful to Dr. Vincent Kofman (NASA GSFC) for kindly sharing a template configuration file for HWO simulations in PSG and for his invaluable assistance through numerous productive discussions on PSG-based simulations. L.M. also thanks Dr. Tyler D. Robinson (University of Arizona) for providing the EPOXI observational data and the parameters used in his work, which significantly aided our discussion of the EPOXI observations of Earth. We further thank Dr. Daniel Angerhausen (ETH Zurich) for his guidance on the LIFE noise simulations. L.M. acknowledges funding support from the DAE through the NISER project RNI 4011. L.M. also thanks Dr. Vishal Gajjar (SETI Institute) for stimulating discussions on biosignatures and technosignatures, which led to the NISER–SETI collaboration. This work was supported in part by Breakthrough Listen at the University of Oxford, through a sub-award to NISER under Agreement R82799/CN013, as part of a global collaboration funded by the Breakthrough Prize Foundation. D.B.P. extends her heartfelt thanks to Swadhin Satapathy, Dwaipayan Dubey, and Rahul Arora for their valuable discussions and guidance at SEPS, NISER. O.P.J. expresses sincere gratitude to Sarin C. Jacob for his assistance. We thank the anonymous referee for constructive comments that improved this manuscript.

Facilities: HWO, LIFE

Software: PSG (Villanueva et al. 2018; Villanueva et al. 2022), LIFEsim (Dannert et al. 2022), NWP <https://nwp-saf.eumetsat.int/site/software/atmospheric-profile-data/>, VULCAN (Tsai et al. 2021), NumPy (Harris et al. 2020), matplotlib (Hunter 2007), pandas (McKinney et al. 2010)

REFERENCES

Alei, E., Konrad, B. S., Angerhausen, D., et al. 2022, *A&A*, 665, A106, doi: [10.1051/0004-6361/202243760](https://doi.org/10.1051/0004-6361/202243760)

Alei, E., Quanz, S. P., Konrad, B. S., et al. 2024, Large Interferometer For Exoplanets (LIFE): XIII. The Value of Combining Thermal Emission and Reflected Light for the Characterization of Earth Twins. <https://arxiv.org/abs/2406.13037>

Angel, J. R. P., & Woolf, N. J. 1997, *The Astrophysical Journal*, 475, 373, doi: [10.1086/303529](https://doi.org/10.1086/303529)

Angerhausen, D., Pidhorodetska, D., Leung, M., et al. 2024, *The Astronomical Journal*, 167, 128, doi: [10.3847/1538-3881/ad1f4b](https://doi.org/10.3847/1538-3881/ad1f4b)

Arney, G. N., Meadows, V. S., Domagal-Goldman, S. D., Claire, M., & Schwieerman, E. 2014, in AGU Fall Meeting Abstracts, Vol. 2014, PP53A–1202

Atkinson, R., Baulch, D. L., Cox, R. A., et al. 2004, *Atmospheric Chemistry and Physics*, 4, 1461, doi: [10.5194/acp-4-1461-2004](https://doi.org/10.5194/acp-4-1461-2004)

Barnes, I., Bastian, V., Becker, K., Fink, E., & Zabel, F. 1981, *Chemical Physics Letters*, 83, 459, doi: [https://doi.org/10.1016/0009-2614\(81\)85501-7](https://doi.org/10.1016/0009-2614(81)85501-7)

—. 1982, *Atmospheric Environment* (1967), 16, 545, doi: [https://doi.org/10.1016/0004-6981\(82\)90163-9](https://doi.org/10.1016/0004-6981(82)90163-9)

Bracewell, R. N. 1978, *Nature*, 274, 780, doi: [10.1038/274780a0](https://doi.org/10.1038/274780a0)

Catling, D. C., Zahnle, K. J., & McKay, C. P. 2001, *Science*, 293, 839, doi: [10.1126/science.1061976](https://doi.org/10.1126/science.1061976)

Chang, J.-s., Trevor, P. L., & Barker, J. R. 1981, *International Journal of Chemical Kinetics*, 13, 1151, doi: <https://doi.org/10.1002/kin.550131106>

Charbonneau, D., Brown, T. M., Noyes, R. W., & Gilliland, R. L. 2002, *The Astrophysical Journal*, 568, 377, doi: [10.1086/338770](https://doi.org/10.1086/338770)

Charbonneau, D., Knutson, H. A., Barman, T., et al. 2008, *The Astrophysical Journal*, 686, 1341, doi: [10.1086/591635](https://doi.org/10.1086/591635)

Chevallier, F., Di Michele, S., & McNally, A. P. 2006, Diverse profile datasets from the ECMWF 91-level short-range forecasts (European Centre for Medium-Range Weather Forecasts)

Currie, T., Biller, B., Lagrange, A.-M., et al. 2023, Direct Imaging and Spectroscopy of Extrasolar Planets. <https://arxiv.org/abs/2205.05696>

Damiano, M., & Hu, R. 2022, *The Astronomical Journal*, 163, 299, doi: [10.3847/1538-3881/ac6b97](https://doi.org/10.3847/1538-3881/ac6b97)

Dannert, F. A., Ottiger, M., Quanz, S. P., et al. 2022, *A&A*, 664, A22, doi: [10.1051/0004-6361/202141958](https://doi.org/10.1051/0004-6361/202141958)

Defrère, D., Léger, A., Absil, O., et al. 2018, *Experimental Astronomy*, 46, 543

Eresmaa, R., & McNally, A. P. 2014, NWP SAF NWPSAF-ECTR-017, 10, 4476

Feng, Y. K., Robinson, T. D., Fortney, J. J., et al. 2018, *The Astronomical Journal*, 155, 200, doi: [10.3847/1538-3881/aab95c](https://doi.org/10.3847/1538-3881/aab95c)

Fortney, J. J. 2024, arXiv preprint arXiv:2405.04587

Fujii, Y., Angerhausen, D., Deitrick, R., et al. 2018, *Astrobiology*, 18, 739, doi: [10.1089/ast.2017.1733](https://doi.org/10.1089/ast.2017.1733)

Gordon, I. E., Rothman, L. S., Hargreaves, R. J., et al. 2022, *JQSRT*, 277, 107949, doi: [10.1016/j.jqsrt.2021.107949](https://doi.org/10.1016/j.jqsrt.2021.107949)

Greene, T. P., Bell, T. J., Ducrot, E., et al. 2023, *Nature*, 618, 39, doi: [10.1038/s41586-023-05951-7](https://doi.org/10.1038/s41586-023-05951-7)

Guermat, C. A. 2018, *Solar Energy*, 169, 434, doi: <https://doi.org/10.1016/j.solener.2018.04.067>

Harris, C. R., Millman, K. J., van der Walt, S. J., et al. 2020, *Nature*, 585, 357, doi: [10.1038/s41586-020-2649-2](https://doi.org/10.1038/s41586-020-2649-2)

Hu, R., Seager, S., & Bains, W. 2012, *The Astrophysical Journal*, 761, 166, doi: [10.1088/0004-637X/761/2/166](https://doi.org/10.1088/0004-637X/761/2/166)

Huebner, W. F., & Carpenter, C. W. 1979, Solar photo rate coefficients

Huebner, W. F., Keady, J. J., & Lyon, S. P. 1992, *Ap&SS*, 195, 1, doi: [10.1007/BF00644558](https://doi.org/10.1007/BF00644558)

Hunter, J. D. 2007, *Computing in Science & Engineering*, 9, 90, doi: [10.1109/MCSE.2007.55](https://doi.org/10.1109/MCSE.2007.55)

Kammerer, J., Quanz, S. P., & Dannert, F. 2022, *Astronomy & Astrophysics*, 668, A52, doi: [10.1051/0004-6361/202243846](https://doi.org/10.1051/0004-6361/202243846)

Kempton, E. M. R., Zhang, M., Bean, J. L., et al. 2023, *Nature*, 620, 67, doi: [10.1038/s41586-023-06159-5](https://doi.org/10.1038/s41586-023-06159-5)

Kleinböhl, A., Willacy, K., Friedson, A. J., Chen, P., & Swain, M. R. 2018, *The Astrophysical Journal*, 862, 92, doi: [10.3847/1538-4357/aaca36](https://doi.org/10.3847/1538-4357/aaca36)

Konrad, B. S., Alei, E., Quanz, S. P., et al. 2022, *Astronomy & Astrophysics*, 664, A23, doi: [10.1051/0004-6361/202141964](https://doi.org/10.1051/0004-6361/202141964)

Konrad, B. S., Alei, E., Quanz, S. P., et al. 2023, *A&A*, 673, A94, doi: [10.1051/0004-6361/202245655](https://doi.org/10.1051/0004-6361/202245655)

Krissansen-Totton, J., Olson, S., & Catling, D. C. 2018, *Science Advances*, 4, eaao5747, doi: [10.1126/sciadv.aao5747](https://doi.org/10.1126/sciadv.aao5747)

Lagrange, A.-M., Bonnefoy, M., Chauvin, G., et al. 2010, *Science*, 329, 57, doi: [10.1126/science.1187187](https://doi.org/10.1126/science.1187187)

Latouf, N., Mandell, A. M., Villanueva, G. L., et al. 2023, *AJ*, 166, 129, doi: [10.3847/1538-3881/acebc3](https://doi.org/10.3847/1538-3881/acebc3)

—. 2024, *AJ*, 167, 27, doi: [10.3847/1538-3881/ad0fde](https://doi.org/10.3847/1538-3881/ad0fde)

Lissauer, J. J., Dawson, R. I., & Tremaine, S. 2014, *Nature*, 513, 336, doi: [10.1038/nature13781](https://doi.org/10.1038/nature13781)

López-Morales, M., Currie, T., Teske, J., et al. 2019, Detecting Earth-like Biosignatures on Rocky Exoplanets around Nearby Stars with Ground-based Extremely Large Telescopes. <https://arxiv.org/abs/1903.09523>

MacLeod, H., Smith, G. P., & Golden, D. M. 1988, *Journal of Geophysical Research: Atmospheres*, 93, 3813, doi: <https://doi.org/10.1029/JD093iD04p03813>

Madhusudhan, N. 2019, *ARA&A*, 57, 617, doi: [10.1146/annurev-astro-081817-051846](https://doi.org/10.1146/annurev-astro-081817-051846)

—. 2025, arXiv e-prints, arXiv:2503.22990, doi: [10.48550/arXiv.2503.22990](https://doi.org/10.48550/arXiv.2503.22990)

Marois, C., Macintosh, B., Barman, T., et al. 2008, *Science*, 322, 1348, doi: [10.1126/science.1166585](https://doi.org/10.1126/science.1166585)

McKinney, W., et al. 2010, in *Proceedings of the 9th Python in Science Conference*, Vol. 445, Austin, TX, 51–56

Meadows, V. S. 2017, *Astrobiology*, 17, 1022, doi: [10.1089/ast.2016.1578](https://doi.org/10.1089/ast.2016.1578)

Meadows, V. S., Reinhard, C. T., Arney, G. N., et al. 2018, *Astrobiology*, 18, 630, doi: [10.1089/ast.2017.1727](https://doi.org/10.1089/ast.2017.1727)

National Academies of Sciences, Engineering, and Medicine. 2021, *Pathways to Discovery in Astronomy and Astrophysics for the 2020s* (Washington, DC: The National Academies Press), doi: [10.17226/26141](https://doi.org/10.17226/26141)

Quanz, S. P., Kammerer, J., Defrre, D., et al. 2018, in *Optical and Infrared Interferometry and Imaging VI*, Vol. 10701, SPIE, 415–431

Quanz, S. P., Absil, O., Benz, W., et al. 2021, *Experimental astronomy*, 1

Quanz, S. P., Absil, O., Benz, W., et al. 2022a, *Experimental Astronomy*, 54, 1197, doi: [10.1007/s10686-021-09791-z](https://doi.org/10.1007/s10686-021-09791-z)

Quanz, S. P., Ottiger, M., Fontanet, E., et al. 2022b, *A&A*, 664, A21, doi: [10.1051/0004-6361/202140366](https://doi.org/10.1051/0004-6361/202140366)

—. 2022c, *A&A*, 664, A21, doi: [10.1051/0004-6361/202140366](https://doi.org/10.1051/0004-6361/202140366)

Robinson, T. D., & Reinhard, C. T. 2019, *Earth as an Exoplanet*. <https://arxiv.org/abs/1804.04138>

Robinson, T. D., & Salvador, A. 2023, *The Planetary Science Journal*, 4, 10, doi: [10.3847/PSJ/acac9a](https://doi.org/10.3847/PSJ/acac9a)

Robinson, T. D., Meadows, V. S., Crisp, D., et al. 2011, *Astrobiology*, 11, 393, doi: [10.1089/ast.2011.0642](https://doi.org/10.1089/ast.2011.0642)

Sagan, C., Thompson, W. R., Carlson, R., Gurnett, D., & Hord, C. 1993, *Nature*, 365, 715

Schwieterman, E. W., & Leung, M. 2024, *An Overview of Exoplanet Biosignatures*. <https://arxiv.org/abs/2404.15431>

Schwieterman, E. W., Kiang, N. Y., Parenteau, M. N., et al. 2018, *Astrobiology*, 18, 663, doi: [10.1089/ast.2017.1729](https://doi.org/10.1089/ast.2017.1729)

Schwieterman, E. W., Olson, S. L., Pidhorodetska, D., et al. 2022, *The Astrophysical Journal*, 937, 109, doi: [10.3847/1538-4357/ac8cfb](https://doi.org/10.3847/1538-4357/ac8cfb)

Seager, S., & Deming, D. 2010, *Annual Review of Astronomy and Astrophysics*, 48, 631

Sing, D. K., Pont, F., Aigrain, S., et al. 2011, *Monthly Notices of the Royal Astronomical Society*, 416, 1443

Smith, C. A., Molina, L. T., Lamb, J. J., & Molina, M. J. 1984, *International Journal of Chemical Kinetics*, 16, 41, doi: <https://doi.org/10.1002/kin.550160107>

Tsai, S.-M., Malik, M., Kitzmann, D., et al. 2021, *ApJ*, 923, 264, doi: [10.3847/1538-4357/ac29bc](https://doi.org/10.3847/1538-4357/ac29bc)

Villanueva, G. L., Liuzzi, G., Faggi, S., et al. 2022, *Fundamentals of the Planetary Spectrum Generator* (Greenbelt, MD: NASA Goddard Space Flight Center)

Villanueva, G. L., Smith, M. D., Protopapa, S., Faggi, S., & Mandell, A. M. 2018, *JQSRT*, 217, 86, doi: [10.1016/j.jqsrt.2018.05.023](https://doi.org/10.1016/j.jqsrt.2018.05.023)

Wesely, M. 1989, *Atmospheric Environment* (1967), 23, 1293, doi: [https://doi.org/10.1016/0004-6981\(89\)90153-4](https://doi.org/10.1016/0004-6981(89)90153-4)

Williams, D. M., & Gaidos, E. 2008, *Icarus*, 195, 927–937, doi: [10.1016/j.icarus.2008.01.002](https://doi.org/10.1016/j.icarus.2008.01.002)

Young, A. V., Crouse, J., Arney, G., et al. 2024, *The Planetary Science Journal*, 5, 7, doi: [10.3847/PSJ/ad09b1](https://doi.org/10.3847/PSJ/ad09b1)

Zurlo, A. 2024, *Direct imaging of exoplanets*. <https://arxiv.org/abs/2404.05797>